Communications in Applied Mathematics and Computational Science

A THEORETICAL STUDY OF AQUEOUS HUMOR SECRETION BASED ON A CONTINUUM MODEL COUPLING ELECTROCHEMICAL AND FLUID-DYNAMICAL TRANSMEMBRANE MECHANISMS

LORENZO SALA, AURELIO GIANCARLO MAURI, RICCARDO SACCO, DARIO MESSENIO, GIOVANNA GUIDOBONI AND ALON HARRIS

vol. 14 no. 1 2019

msp

COMM. APP. MATH. AND COMP. SCI.
Vol. 14, No. 1, 2019
dx.doi.org/10.2140/camcos.2019.14.65

msp

A THEORETICAL STUDY OF AQUEOUS HUMOR SECRETION BASED ON A CONTINUUM MODEL COUPLING ELECTROCHEMICAL AND FLUID-DYNAMICAL TRANSMEMBRANE MECHANISMS

LORENZO SALA, AURELIO GIANCARLO MAURI, RICCARDO SACCO, DARIO MESSENIO, GIOVANNA GUIDOBONI AND ALON HARRIS

Intraocular pressure, resulting from the balance of aqueous humor (AH) production and drainage, is the only approved treatable risk factor in glaucoma. AH production is determined by the concurrent function of ion pumps and aquaporins in the ciliary processes, but their individual contribution is difficult to characterize experimentally. In this work, we propose a novel unified modeling and computational framework for the finite element simulation of the role of the main ion pumps and exchangers involved in AH secretion, namely, the sodium-potassium pump, the calcium-sodium exchanger, the chloride-bicarbonate exchanger, and the sodium-proton exchanger. The theoretical model is developed at the cellular scale and is based on the coupling between electrochemical and fluid-dynamical transmembrane mechanisms characterized by a novel description of the electric pressure exerted by the ions on the intrapore fluid that includes electrochemical and osmotic corrections. Considering a realistic geometry of the ion pumps, the proposed model is demonstrated to correctly predict their functionality as a function of (1) the permanent electric charge density over the pore surface, (2) the osmotic gradient coefficient, and (3) the stoichiometric ratio between the ion pump currents enforced at the inlet and outlet sections of the pore. In particular, theoretical predictions of the transepithelial membrane potential for each simulated pump/exchanger allow us to perform a first significant model comparison with experimental data for monkeys. This is a significant step for future multidisciplinary studies on the action of molecules on AH production.

1. Introduction

The flow of aqueous humor (AH) and its regulation play an important role in ocular physiology by contributing to control the level of intraocular pressure (IOP) [36; 28]. Elevated IOP is the only approved treatable risk factor in glaucoma, an

MSC2010: primary 35K59, 65M60, 76D07, 92C35, 92C37; secondary 76Z05.
Keywords: ion exchangers, eye, ion pumps, aqueous humor, mathematical modeling, simulation, finite element method.

optic neuropathy characterized by a multifactorial aetiology with a progressive degeneration of retinal ganglion cells that ultimately leads to irreversible vision loss [18; 59]. Currently, glaucoma affects more than 60 million people worldwide and is estimated to reach almost 80 million by 2020 [38]. IOP can be lowered via hypotonizing eye drops and/or surgical treatment, and it can be shown that reducing IOP by 1 mmHg has the effect of reducing the risk of glaucoma progression and subsequent vision loss by 10% [19].

Several classes of IOP-lowering medications are available for use in patients with glaucoma, including prostaglandin analogues, beta-blockers, carbonic anhydrase inhibitors, and alpha-2-adrenergic agonists, in fixed and variable associations, while newer classes are still in clinical trials, such as the rho kinase inhibitors [17; 21; 39]. All currently available IOP-lowering agents function by altering AH production or drainage. However, differences in drug efficacy have been observed among patients that cannot be completely explained without a clear understanding of the mechanisms regulating AH flow. Motivated by this need, in this work we focus on AH production and we propose a mathematical approach to model and simulate the contribution of ion pumps and exchanger to determine AH flow.

The production of AH takes places in the ciliary processes within the ciliary body, where clear liquid flows across the ciliary epithelium, a two-layered structure composed of an inner nonpigmented layer, representing the continuation of retinal pigmented epithelium, and an external nonpigmented layer, representing the continuation of the retina [16], as illustrated in Figure 1.

Three main mechanisms are involved in the production of AH: (i) convective delivery of fluid and metabolic components via the ciliary circulation, (ii) ultrafiltration and diffusion of fluid and metabolic components across the epithelial cells driven by gradients in hydrostatic pressure, oncotic pressure, and metabolite concentrations, and (iii) active secretion into the posterior chamber driven by increased ion concentrations within the basolateral space between nonpigmented epithelial cells.

In this work we focus on the third mechanism, henceforth referred to as *AH secretion*, which is responsible for approximately 80–90% of the whole AH production process [15; 32]. More precisely, we aim to model the selective movement of anions and cations across the membrane of the nonpigmented epithelial cells, the resulting gradient of ion and solute concentrations across the membrane, and the induced fluid egression into the posterior chamber.

The proposed simulation of AH secretion presents many challenges from the modeling viewpoint. Existing references concerning AH secretion are primarily based on lumped parameter models that provide a systemic view of AH flow [7; 29; 52], but do not reproduce the detailed phenomena occurring at the level of single ion pumps and exchangers. Detailed models based on the velocity-extended Poisson–Nernst–Planck (VE-PNP) system have been utilized to simulate electrokinetic flows

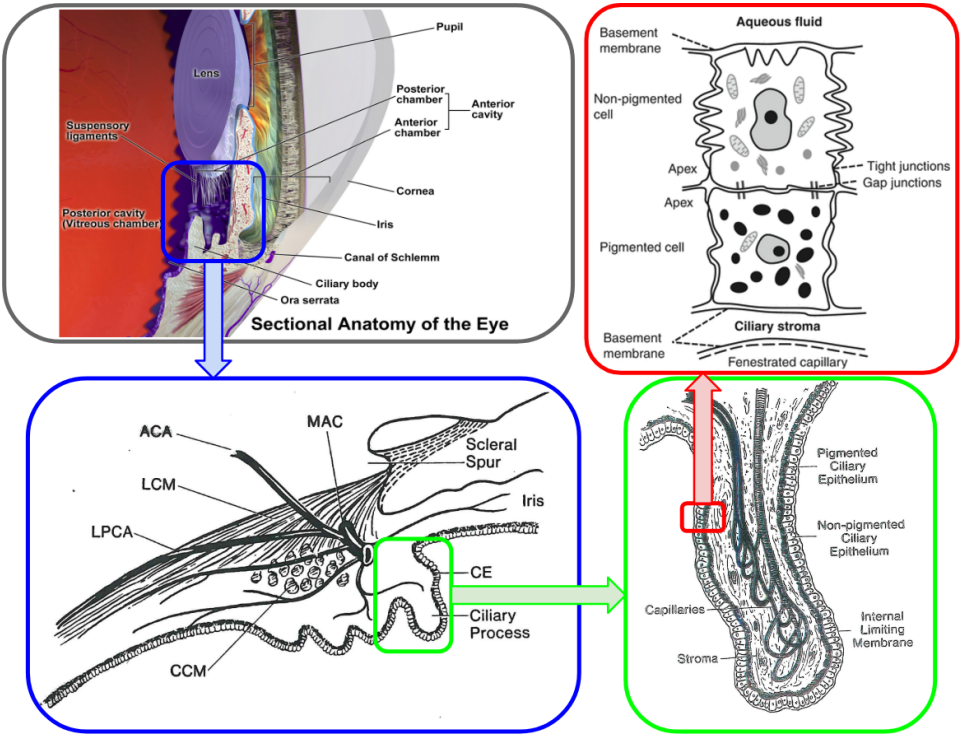

Figure 1. Left top: anatomy of the eye and of the structures involved in aqueous humor production and regulation [5]. Left bottom: MAC: major arterial circle; ACA: anterior ciliary arteries; LPCA: long posterior ciliary artery; LCM: longitudinal (fibers) ciliary muscle; CCM: circular (fibers) ciliary muscle; CE: ciliary epithelium (figure reproduced from [49]). Right bottom: a ciliary process is composed of capillaries, stroma, and two layers of epithelium (inner, pigmented and outer, nonpigmented) (figure reproduced from [49]). Right top: the two-layer structure of the ciliary epithelium (figured reproduced from [56]).

[26; 3; 4], but different models for the volumetric force coupling electrochemical and fluid-dynamical mechanisms have been proposed [51; 41; 42; 13], thereby raising the question of which one, if any, is the most appropriate for the application at hand. In addition, some of the most important parameters in the VE-PNP model, such as the concentration of ions within the pore, the fixed charge on the pore lateral surface, and the osmotic diffusive parameter, cannot be easily accessed experimentally and so are not readily available in the literature. In the pilot investigation conducted in [35], we explored the feasibility of utilizing a VE-PNP model to simulate the sodium-potassium pump (Na^+-K^+) within the nonpigmented epithelial cells of the eye. However, several other ion pumps and exchangers are involved in AH secretion [28], and have not yet been modeled in the context of AH flow.

The present work aims at extending the modeling and simulation treatment of [35] through the development of a unified framework capable of simulating

AH secretion by including the four main ion pumps and exchangers involved in the process, namely, the calcium-sodium exchanger (Ca^{++}-Na^{+}), the chloride-bicarbonate exchanger (Cl^{-}-HCO_3^{-}), and sodium-proton exchanger (Na^{+}-H^{+}). The computational structure used in the numerical simulations is based on the adoption of (1) a temporal semidiscretization with the backward Euler method, (2) a Picard iteration to successively solve the equation system at each discrete time level, and (3) a spatial discretization of each differential subproblem obtained from system decoupling using the Galerkin finite element method.

Remark. The present work focuses on the study of the system when steady-state conditions are reached.

Numerical simulations are utilized to (i) compare how and to what extent different modeling choices for the volumetric coupling force affect the resulting transmembrane potential, stoichiometric ratio, and intrapore fluid velocity and (ii) characterize the correct boundary conditions and the value of the permanent electric charge density on the pore lateral surface that allow us to predict a biophysically reasonable behavior of ion pumps and exchangers in realistic geometries. Overall, this work provides the first systematic investigation of VE-PNP models in the context of AH secretion and paves the way to future studies on biochemical, pharmacological, and therapeutic aspects of AH flow regulation.

The paper is organized as follows. Section 2 provides a brief functional description of the main features pertaining to the Na^{+}-K^{+} pump and the Ca^{++}-Na^{+}, Cl^{-}-HCO_3^{-}, and Na^{+}-H^{+} exchangers. The VE-PNP system is described in Section 3, and the mathematical model for the volume force density in the right-hand side of the linear momentum balance equation for the intrapore fluid is described in Section 4. The numerical discretization of the VE-PNP model equations is discussed in Section 5, whereas simulation results of the effect of volumetric forces and permanent electric charge density are presented in Sections 6 and 7, respectively. Model limitations, conclusions, and future perspectives are outlined in Section 8.

2. Ion pumps and exchangers in AH secretion

In this section we provide a short description of the main ion pumps and exchangers that are involved in the process of AH secretion. A schematic representation of these ion pumps and exchangers is illustrated in Figure 2. We refer to [20] for an overview of ion pumps and exchangers in cellular biology and to [27] for their mathematical treatment.

The sodium-potassium pump. This pump plays a fundamental role in cellular biology as it is present in the membrane of every cell in the human body. The enzyme ATPase, located either in pigmented or nonpigmented ciliary epithelium,

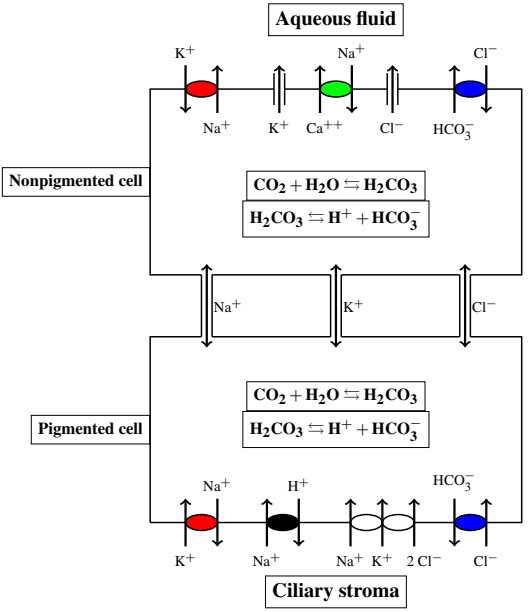

Figure 2. Schematic diagram of ion pumps and exchangers located on the lipid membrane in the nonpigmented epithelial cells of the ciliary body of the eye. Aqueous humor is produced by the active secretion of fluid through the ion pumps and exchangers during their activity. This figure is inspired by Figure 9 of [48].

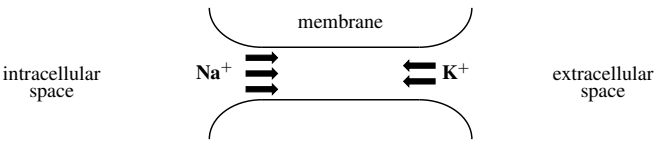

Figure 3. Schematic representation of the Na^+-K^+ pump. The stoichiometric ratio is 3 : 2, since there is an outflux of three Na^+ ions and an influx of two K^+ ions.

causes the hydrolysis of one molecule of ATP and produces the necessary energy to expel three Na^+ ions, while allowing two K^+ ions to enter. This process is not electrically neutral as it entails an outflux of three positive charged particles of sodium and an influx of only two positive charged particles of potassium. The ion outflux and influx are schematically represented in Figure 3.

The calcium-sodium exchanger. This exchanger is activated when calcium accumulates inside the cell above a certain threshold that is usually around 1 mM. It entails the influx of three Na^+ ions and an outflux of one Ca^{++} ion. As in the previous case, this process is not electrically neutral as three positive sodium ions enter the cell whereas only one positive calcium ion exits the cell. The ion outflux and influx are schematically represented in Figure 4.

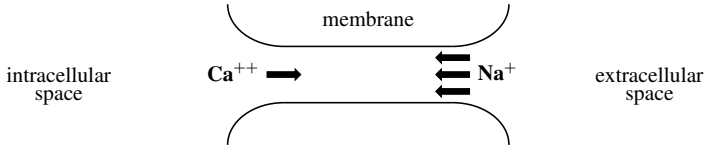

Figure 4. Schematic representation of the Ca^{++}-Na^{+} pump. The stoichiometric ratio is 3 : 1, since there is an influx of three Na^{+} ions and an outflux of one Ca^{++} ion.

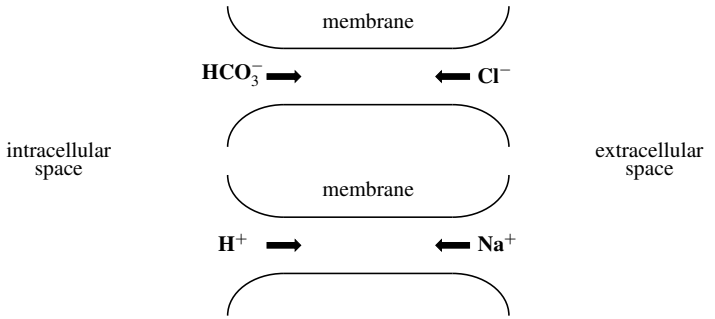

Figure 5. Schematic representation of the chloride-bicarbonate (top) and the sodium-proton exchangers (bottom). The stoichiometric ratio of the chloride-bicarbonate exchanger is 1 : 1, since there is an influx of one Cl^{-} ion and an outflux of one HCO_3^{-} ion. The stoichiometric ratio of the sodium-proton exchanger is also 1:1, since there is an influx of one Na^{+} ion and an outflux of one H^{+} ion.

The chloride-bicarbonate exchanger. This exchanger involves the movement of negative ions. Carbonic anhydrase is an enzyme that mediates the transport of bicarbonate across the ciliary epithelium to maintain the homeostatic balance of carbonate across the cell membrane. More precisely, carbonic anhydrase favors the splitting of one molecule of H_2CO_3 into a positive H^{+} ion and a negative HCO_3^{-} ion. Then, the HCO_3^{-} ion exits the cell through the pore with an exchange of a chlorine ion Cl^{-} that enters the cell. The balance of this exchanger is electrically neutral because for every negative charged HCO_3^{-} leaving the cell there is a negative charged Cl^{-} ion entering the cell [58]. The ion outflux and influx are schematically represented in the top panel of Figure 5.

The sodium-proton exchanger. This exchanger is strictly correlated with the activity of the chloride-bicarbonate exchanger previously described. A positive H^{+} ion resulting from the splitting reaction of one molecule of H_2CO_3 exits the cell with an exchange of one Na^{+} ion entering the cell. Thus, this exchanger is electrically neutral. The ion outflux and influx are schematically represented in the bottom panel of Figure 5.

3. The mathematical model

In this section we illustrate the system of partial differential equations (PDEs) constituting the mathematical model at the cellular scale level of ion pumps and exchangers that activate the AH secretion. We refer to [45] for a detailed discussion of the analytical properties of the model equations and of the numerical methods used for their discretization, and to [35] for preliminary results on the adoption of the model in the study of the role of bicarbonate ion to correctly determine the electrostatic potential drop across the cellular membrane at the level of eye transepithelium.

The geometrical setting that we consider henceforth is the computational domain Ω illustrated in Figure 6 representing a cross-section of a simplified pore geometry.

Remark. The pore geometry for real ion pumps is much more complex than the simple cylinder depicted in Figure 6. It has also been observed that the pore geometry might vary during the activity of the pump [60]. Even though a more complicated geometry is considered in Section 7, the present work has to be considered as a first step towards more realistic geometric settings.

Such representation includes any of the ion pumps and exchangers described in Section 2, which are located on the lipid bilayer constituting the membrane of the nonpigmented epithelial cells of the ciliary body of the eye schematically depicted in Figure 1 (right top). We indicate by $\partial\Omega$ the boundary of Ω, by $\underline{n}$ the outward unit normal vector on $\partial\Omega$, and by sideA, sideB, and Γ_{LAT} the intracellular surface, the extracellular surface, and the lateral boundary, respectively, in such a way that $\partial\Omega = \mathrm{sideA} \cup \mathrm{sideB} \cup \Gamma_{\mathrm{LAT}}$. For a given starting time t_0 and a given observational time window T_{obs}, we set $I_T := (t_0, t_0 + T_{\mathrm{obs}})$ and we denote by $Q_T := \Omega \times I_T$ the space-time cylinder in which we study the spatial and temporal evolution of the process of AH secretion at the cellular scale level. To clarify the physical foundation of the cellular scale model object of the present article, we assume that the following strongly coupled mechanisms concur to determine AH secretion:

electric field formation. This mechanism is determined by the mutual interaction among ions in the intrapore fluid and their interaction with the permanent electric charge density distributed on the surface of the pore structure. Mathematically, the mechanism is described by the Poisson equation, supplied by appropriate boundary conditions at the inlet and outlet sections of the pore and on its external surface.

ion motion. This mechanism is determined by the superposition of a diffusion process driven by ion concentration gradients along the pore and of a drift process driven by the force exerted by the electric field on each ion charged particle. Mathematically, the mechanism is described by the Nernst–Planck

equations, supplied by appropriate initial conditions inside the pore and by appropriate boundary conditions at the inlet and outlet sections of the pore and on its external surface.

fluid motion. This mechanism is determined by the volume force density that is exerted by the charged ion particles because of their motion inside the pore. Mathematically, the mechanism is described by the time-dependent Stokes equations, supplied by appropriate initial conditions inside the pore and by appropriate boundary conditions at the inlet and outlet sections of the pore and on its external surface.

We refer to the resulting mathematical model as *velocity-extended Poisson–Nernst–Planck* system (VE-PNP) [44; 24; 47; 25]. The VE-PNP system can be derived by the application of the following physical laws [45]: (i) mass balance for each of the M chemical species included in the system (1a), (ii) linear momentum balance for each chemical species (1b), (iii) electric charge conservation (1c), (iv) mass balance for intrapore fluid (1e), and (v) linear momentum balance for the mixture of intrapore fluid and ion species (1f). Ultimately, the system consists of the following set of PDEs to be solved in Q_T:

$$\frac{\partial n_i}{\partial t} + \operatorname{div} \underline{f}_i = 0 \qquad \text{for all } i = 1, \dots, M, \tag{1a}$$

$$\underline{f}_i = \frac{z_i}{|z_i|}\mu_i n_i \underline{E} - D_i \nabla n_i + \boxed{n_i \underline{u}} \qquad \text{for all } i = 1, \dots, M, \tag{1b}$$

$$\operatorname{div}(-\epsilon_f \nabla \varphi) = q \sum_{i=1}^{M} z_i n_i + q\rho_{\text{fixed}}, \tag{1c}$$

$$\underline{E} = -\nabla \varphi, \tag{1d}$$

$$\operatorname{div} \underline{u} = 0, \tag{1e}$$

$$\rho_f \frac{\partial \underline{u}}{\partial t} = \operatorname{div} \underline{\underline{\sigma}}(\underline{u}, p) + \boxed{\underline{F}_{\text{ion}}}, \tag{1f}$$

$$\underline{\underline{\sigma}}(\underline{u}, p) = 2\mu_f \underline{\underline{S}}(\underline{u}) - p\, \underline{\underline{\delta}}, \tag{1g}$$

$$\underline{\underline{S}}(\underline{u}) = \underline{\underline{\nabla}}_s \underline{u} = \tfrac{1}{2}(\nabla \underline{u} + (\nabla \underline{u})^T). \tag{1h}$$

The equation set (1) comprises two main blocks. Equations (1a)–(1d) constitute the Poisson–Nernst–Planck (PNP) block whereas (1e)–(1h) constitute the Stokes block. As far as the PNP block is concerned, M is the number of ion species, $\underline{f}_i$ denotes the ion particle flux [$\mathrm{cm}^{-2}\,\mathrm{s}^{-1}$], n_i is the ion concentration [cm^{-3}], and μ_i and D_i are the ion electric mobility [$\mathrm{cm}^2\,\mathrm{V}\,\mathrm{s}^{-1}$] and diffusivity [$\mathrm{cm}^2\,\mathrm{s}^{-1}$], respectively. The mobility μ_i is proportional to the diffusivity D_i through the

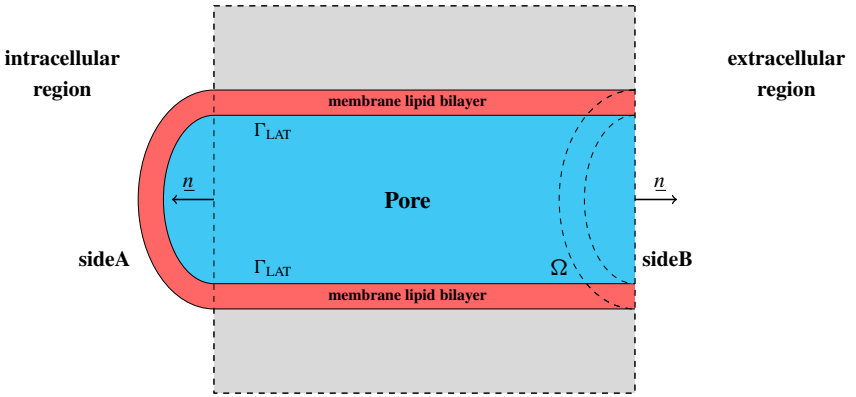

Figure 6. Cross-section of a simplified pore geometry. The lipid membrane bilayer is represented in brown color. The pore is represented in cyan color. The portions of the boundary $\partial\Omega$ are labeled as sideA (intracellular side), sideB (extracellular side), and Γ_{LAT} (lateral surface).

Einstein relation

$$D_i = \frac{K_B T}{q|z_i|}\mu_i, \quad i = 1, \ldots, M, \tag{2}$$

where q is the electron charge [C], K_B is the Boltzmann constant [$\text{cm}^2\,\text{g}\,\text{s}^{-2}\,\text{K}^{-1}$], and T is the absolute temperature [K]. In (1c) and (1d), $\underline{E}$ is the electric field [$\text{V}\,\text{cm}^{-1}$], φ is the electric potential [V], and ϵ_f is the electrolyte fluid dielectric permittivity [$\text{F}\,\text{cm}^{-1}$]. The quantity z_i is the valence of the i-th ion ($z_i > 0$ for cations, $z_i < 0$ for anions) whereas ρ_{fixed} is the permanent electric charge density [$\text{C}\,\text{cm}^{-3}$]. We define the ion current density $\underline{J}_i$ [$\text{A}\,\text{cm}^{-2}$] of each ion species as

$$\underline{J}_i = q z_i \underline{f}_i, \quad i = 1, \ldots, M. \tag{3}$$

As far as the Stokes block is concerned, $\underline{u}$ is the mixture velocity [$\text{cm}\,\text{s}^{-1}$] and mixture incompressibility is expressed by (1e). Equations (1g) and (1h) are the constitutive laws for the stress tensor [$\text{dyne}\,\text{cm}^{-2}$] and the strain rate [$\text{s}^{-1}$], respectively, where p denotes the mixture pressure [$\text{dyne}\,\text{cm}^{-2}$], μ_f is the mixture viscosity [$\text{g}\,\text{cm}^{-1}\,\text{s}^{-1}$], ρ_f is the mixture mass density [$\text{g}\,\text{cm}^{-3}$], and $\underline{\underline{\delta}}$ the second-order identity tensor of dimension 3. Since the focus of the article is the investigation of the role of electrochemical forces on the secretion of AH across the nonpigmented epithelial cells in the ciliary body of the eye, we assume that the temperature T of the intrapore mixture is constant and equal to the value $T_0 = 293.75\,\text{K}$ and we will refer to the mixture of water and ion species as AH fluid. The boxed terms in (1b) and (1f) are the contributions that introduce the coupling between the PNP block of

system (1) and the Stokes block of system (1). In particular,

$$\underline{F}_{\text{ion}} = \sum_{i=1}^{M} \underline{F}_i \tag{4}$$

expresses the volume force density [dyne cm^{-3}] exerted by the ion charges on the intrapore AH fluid, the quantities $\underline{F}_i$ representing the contribution to the volume force density given by each ion species, $i = 1, \ldots, M$.

The equation system (1) is equipped with the initial conditions

$$n_i(\underline{x}, 0) = n_i^0(\underline{x}), \quad i = 1, \ldots, M, \quad \underline{x} \in \Omega, \tag{5a}$$

$$\underline{u}(\underline{x}, 0) = \underline{u}^0(\underline{x}), \quad \underline{x} \in \Omega, \tag{5b}$$

where n_i^0 are given positive functions and $\underline{u}^0$ is a given function. The initial condition $\varphi^0 = \varphi^0(\underline{x})$, $\underline{x} \in \Omega$, is the solution of the equation set (1c)–(1d), under appropriate boundary conditions on $\partial\Omega$, having set $n_i = n_i^0$, $i = 1, \ldots, M$.

The boundary conditions associated with system (1) that are considered in the present article are of mixed Dirichlet–Neumann type. Their characterization for each equation in the system is specified in each simulation illustrated in Sections 6 and 7.

4. Model for the volume force density

Many approaches have been adopted in the literature to model volume force density dictated by different needs in various contexts. One of the most used force models is the Stratton model [51] for both its simplicity and efficacy. However, more sophisticated modeling approaches are needed to account for microscopic phenomena such as drift and diffusion effects in semiconductor devices [37] or the effect of particle size exclusion that is well described by the hard sphere theory [43; 40]. Our idea is to unify the various volume force models proposed in the literature, compare their different impact in our problem, and select the more appropriate one.

In this section, therefore, we discuss a general approach to the modeling of the volume force density $\underline{F}_i$ on the right-hand side in the linear momentum balance equation (1f). $\underline{F}_i$ expresses the contribution from the i-th ion species, $i = 1, \ldots, M$, to the total volume force density exerted by the ion charged particles on the intrapore fluid and is assumed henceforth to be characterized by the relation

$$\underline{F}_i = q z_i n_i \underline{E}_i^{\text{echs}} - k_{\text{osm}} \nabla n_i, \quad i = 1, \ldots, M. \tag{6}$$

The first term on the right-hand side of (6) represents the volume force density due to a generalized electrochemical field $\underline{E}_i^{\text{echs}}$ whereas the second term represents the volume force density due to an osmotic concentration gradient according to

the parameter k_{osm} [N m] [23]. The generalized electrochemical field is the result of the superposed effect of passive drift due to the electric field (e), the diffusion mechanism associated with a chemical concentration gradient (c), and the particle size exclusion effect associated with the hard sphere (hs) theory [43; 40]. Relation (6) is referred to henceforth as an electrochemical model including osmotic and size exclusion mechanisms (echsk).

Assuming that $\underline{E}_i^{\text{echs}}$ is a gradient field, we have

$$\underline{E}_i^{\text{echs}} = -\nabla\varphi_i^{\text{echs}}, \quad i = 1, \ldots, M, \tag{7a}$$

$$\varphi_i^{\text{echs}} = \varphi_i^{\text{ec}} + \mu_i^{\text{ex}}, \quad i = 1, \ldots, M, \tag{7b}$$

where φ_i^{ec} is the generalized electrochemical potential of the i-th species

$$\varphi_i^{\text{ec}} = \varphi + \frac{V_{\text{th}}}{z_i} \ln\left(\frac{n_i}{n_{\text{ref}}}\right), \quad i = 1, \ldots, M, \tag{7c}$$

and μ_i^{ex} is the exclusion effect potential of the i-th species [6]

$$\begin{aligned}\mu_i^{\text{ex}} = -V_{\text{th}}\Bigg[&\ln\left(1 - \frac{4\pi}{3}\sum_{k=1}^{M} n_k R_k^3\right) \\ &+ 4\pi\,\frac{R_i\left(\sum_{k=1}^{M} n_k R_k^2\right) + R_i^2\left(\sum_{k=1}^{M} n_k R_k\right) + \frac{1}{3}R_i^3\left(\sum_{k=1}^{M} n_k\right)}{1 - (4\pi/3)\sum_{k=1}^{M} n_k R_k^3} \\ &+ \frac{16\pi^2}{3}\,\frac{R_i^3\left(\sum_{k=1}^{M} n_k R_k\right)\left(\sum_{k=1}^{M} n_k R_k^2\right) + \frac{3}{2}R_i^2\left(\sum_{k=1}^{M} n_k R_k^2\right)^2}{\left(1 - (4\pi/3)\sum_{k=1}^{M} n_k R_k^3\right)^2} \\ &+ \frac{64\pi^3}{9}\,\frac{R_i^3\left(\sum_{k=1}^{M} n_k R_k^2\right)^3}{\left(1 - (4\pi/3)\sum_{k=1}^{M} n_k R_k^3\right)^3}\Bigg], \quad i = 1, \ldots, M,\end{aligned} \tag{7d}$$

n_{ref} and R_i being positive constants [cm^{-3}] representing reference concentration and radius of the i-th ion species, respectively. Relation (6) is indeed a general view of the volume force density from which simpler expressions of $\underline{F}_i$ can be derived. These models constitute a hierarchy characterized by an increasing number of approximations and a consequent decreasing level of physical complexity.

echs (*electrochemical model including hard sphere theory*). This model is derived from (6) by neglecting the contribution of the osmotic gradient. This includes the Coulomb electric force associated with a charge density, the chemical gradient, and size exclusion mechanisms. It is mathematically expressed by

$$\underline{F}_i = q z_i n_i \underline{E}_i^{\text{echs}}, \quad i = 1, \ldots, M. \tag{8}$$

ec (*electrochemical model*). This is derived from (8) neglecting the size exclusion phenomena. This includes the Coulomb electric force associated with a charge density and the chemical gradient mechanism. It is mathematically expressed by

$$\underline{F}_i = q z_i n_i \underline{E}_i^{\mathrm{ec}}, \quad i = 1, \ldots, M, \tag{9a}$$

$$\underline{E}_i^{\mathrm{ec}} = -\nabla \varphi_i^{\mathrm{ec}}, \quad i = 1, \ldots, M. \tag{9b}$$

Stratton (*Stratton model*). This model is derived from (9a) by neglecting the contribution induced by the chemical gradient. This was originally proposed in [51], and it is widely adopted in the modeling description of electrokinetic phenomena [26]. It is mathematically expressed by

$$\underline{F}_i = q z_i n_i \underline{E}, \quad i = 1, \ldots, M. \tag{10}$$

eck (*electrochemical model including osmotic force*). This model is derived from (6) by neglecting the contribution of the size exclusion phenomena. This model includes the Coulomb electric force associated with a charge density and the chemical and osmotic gradient mechanisms. It is mathematically expressed by

$$\underline{F}_i = q z_i n_i \underline{E}_i^{\mathrm{ec}} - k_{\mathrm{osm}} \nabla n_i, \quad i = 1, \ldots, M. \tag{11}$$

The effect on intrapore AH fluid motion induced by the above force models is analyzed, in the context of the Na^+-K^- pump, in Section 6 where the predicted electrolyte fluid velocity is compared with the volumetric force density $\underline{F}_i$ exerted by the ions on it.

5. Time advancing, functional iteration, and numerical discretization

In this section we provide a short description of the algorithm that is used to numerically solve system (1). We refer to [45] for more details on the stability and convergence analysis of the adopted methods as well as their implementation in the general-purpose C++ modular numerical code MP-FEMOS (Multi-Physics Finite Element Modeling Oriented Simulator) that has been developed by some of the authors [34; 33; 1].

The VE-PNP model mathematically represents a nonlinearly coupled system of PDEs of incomplete parabolic type because of the fact that at each time level the electrostatic potential φ and the electric field $\underline{E}$ must be updated as a function of the ion concentrations and of the fixed permanent charge by solving the elliptic Poisson equation (1c). In turn, the electric field $\underline{E}$ contributes to determine ion motion through the Nernst–Planck relation (1b) and fluid motion through the relation (6) for the volume force density.

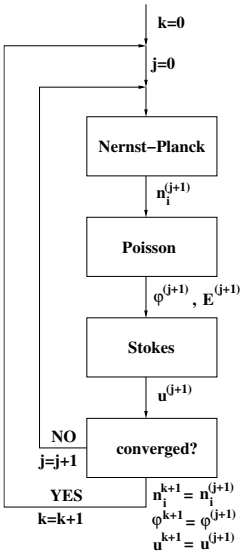

Figure 7. Flowchart of the computational algorithm to solve the VE-PNP system. The nonnegative integer k is the temporal discretization counter. The nonnegative integer j is the Picard iteration counter.

To disentangle the various coupling levels that are present in the VE-PNP system, we proceed as follows:

(1) We perform a temporal semidiscretization of the problem by resorting to the backward Euler (BE) method.

(2) We introduce a Picard iteration to successively solve the equation system at each discrete time level.

(3) We perform a spatial discretization of each differential subproblem obtained from system decoupling using the Galerkin finite element method (GFEM).

The use of the BE method has the twofold advantage that (a) it is unconditionally absolute stable, (b) it is monotone.

Property (a) allows us to take relatively large time steps, thus *reducing the computational effort to reach steady-state conditions*. Property (b) combined with an analogous one for the spatial discretization scheme of the Nernst–Planck equations ensures that the *computed ion concentrations are positive for all discrete time levels*.

The use of a Picard iteration has the twofold advantage that (c) it is a decoupled algorithm and (d) a maximum principle is satisfied by the solutions of two of the boundary value problems (BVPs) obtained from decoupling. Property (c) amounts to transforming the nonlinearly coupled system (1) into the successive solution of three sets of linear BVPs of reduced size. Property (d) implies the existence of an invariant region for the electric potential depending only on the boundary

data and on the fixed permanent charge and the positivity of the computed ion concentrations.

The use of the GFEM has the twofold advantage that (e) it can easily handle complex geometries and (f) provides an accurate and stable numerical approximation of the solution of each BVP obtained from system decoupling. Property (e) is implemented through the partition of the domain of biophysical interest into the union of tetrahedral elements of variable size. Property (f) is implemented through the use of piecewise linear finite elements for the Poisson equation, piecewise linear finite elements with exponential fitting stabilization along of mesh edges for the Nernst–Planck equations, and the inf-sup stable Taylor–Hood finite element pair for the Stokes equations.

Figure 7 illustrates the flowchart of the temporal semidiscretization for time advancing with the BE method and the Picard iteration used to successively solve the three linear equation subsystems.

6. Comparison of volumetric force models on an idealized sodium-potassium pump

The aim of this section is to compare the different descriptions introduced in Section 4 of the volume force density $\underline{F}_{\text{ion}}$ exerted on the intrapore fluid in the linear momentum balance equation (1f). In particular we investigate the biophysical reliability of the various models to describe the functionality of an idealized version of the Na^+-K^+ pump illustrated in Section 2 in which the simultaneous presence of Na^+, K^+, Cl^-, and HCO_3^- ion species is considered. The analysis criteria are based on the comparison of simulation results with (i) the electrostatic potential drop measured across the transepithelial membrane, (ii) the theoretical stoichiometric ratio 3 : 2, and (iii) the direction of the AH flow from the cell into the basolateral space. The ideality of the Na^+-K^+ pump is represented by the geometry adopted for numerical simulation, consisting of the cylinder with axial length $L_{\text{ch}} = 5\,\text{nm}$ and radius $R_{\text{ch}} = 0.4\,\text{nm}$ shown in Figure 8 together with its partition into 37075 tetrahedral finite elements. We point out that the above geometrical setting, despite being a simplified approximation of the real structure, has been successfully employed for biological investigations in [1; 45; 35].

Boundary and initial conditions. Because of the complexity of the boundary conditions (BCs) and initial conditions (ICs) involved in the simulation of the pump, it is useful to accurately describe them for each equation in (1).

Poisson equation. For all $t \in I_T$, the BCs for the Poisson equation (1c)–(1d) are

$$\varphi = 0 \qquad \text{on sideA}, \tag{12a}$$

$$\underline{D} \cdot \underline{n} = 0 \qquad \text{on sideB} \cup \Gamma_{\text{LAT}}. \tag{12b}$$

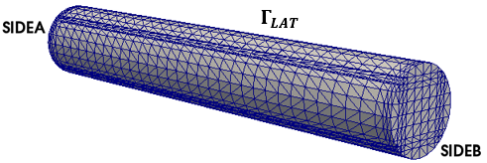

Figure 8. Computational domain for the simulation of the Na^+-K^+ pump. The finite element triangulation consists of 37075 tetrahedra.

Condition (12a) has the scope of introducing a reference value for the calculation of the electrostatic potential drop across the cellular membrane. Condition (12b) expresses the biological fact that the aforementioned potential drop is caused solely by the ion charge distribution within the pore because no external bias is applied.

Nernst–Planck equations. The Nernst–Planck equation system allows us to determine the spatial concentration of the various ion species inside the pore. The connection between the pore region and the intra- and extracellular sides is made possible by enforcing nonhomogeneous Neumann boundary conditions that preserve the correct input/output biophysical pump functionality. The boundary and initial conditions for each simulated ion species read as follows:

$$
\begin{aligned}
&K^+: && \underline{f}_{K^+} \cdot \underline{n} = g_{K^+} && \text{on sideA,} && (13a)\\
& && n_{K^+} = K^+_{out} && \text{on sideB,} && (13b)\\
& && \underline{f}_{K^+} \cdot \underline{n} = 0 && \text{on } \Gamma_{LAT}, && (13c)\\
& && n_{K^+}(\underline{x}, 0) = K^+_0 && \text{for all } \underline{x} \in \Omega, && (13d)\\
&Na^+: && n_{Na^+} = Na^+_{in} && \text{on sideA,} && (13e)\\
& && \underline{f}_{Na^+} \cdot \underline{n} = g_{Na^+} && \text{on sideB,} && (13f)\\
& && \underline{f}_{Na^+} \cdot \underline{n} = 0 && \text{on } \Gamma_{LAT}, && (13g)\\
& && n_{Na^+}(\underline{x}, 0) = Na^+_0 && \text{for all } \underline{x} \in \Omega, && (13h)\\
&Cl^-: && n_{Cl^-} = Cl^-_{in} && \text{on sideA,} && (13i)\\
& && n_{Cl^-} = Cl^-_{out} && \text{on sideB,} && (13j)\\
& && \underline{f}_{Cl^-} \cdot \underline{n} = 0 && \text{on } \Gamma_{LAT}, && (13k)\\
& && n_{Cl^-}(\underline{x}, 0) = Cl^-_0 && \text{for all } \underline{x} \in \Omega, && (13l)\\
&HCO_3^-: && n_{HCO_3^-} = HCO^-_{3,in} && \text{on sideA,} && (13m)\\
& && n_{HCO_3^-} = HCO^-_{3,out} && \text{on sideB,} && (13n)\\
& && \underline{f}_{HCO_3^-} \cdot \underline{n} = 0 && \text{on } \Gamma_{LAT}, && (13o)\\
& && n_{HCO_3^-}(\underline{x}, 0) = HCO^-_{3,0} && \text{for all } \underline{x} \in \Omega. && (13p)
\end{aligned}
$$

The values of the boundary data for the cations are specified in Table 12 whereas the values of the boundary data for the anions are specified in Table 13. The boundary values for the ions agree with the experimental values of the ion concentrations measured in the intracellular and extracellular sides of the nonpigmented epithelial cells [53].

Stokes system. The calculation of AH fluid velocity is made possible by solving the Stokes system (1e)–(1f). To prescribe a correct biophysical condition of the intrapore AH fluid we need to mathematically express that (1) the fluid is adherent to the pore wall, (2) no external pressure drop is applied across the pore, and (3) the AH fluid is at the rest when the pump is not active. To this purpose, the appropriate BCs and ICs read

$$\underline{u} = \underline{0} \quad \text{on } \Gamma_{\text{LAT}}, \tag{14a}$$

$$\underline{\underline{\sigma}}\,\underline{n} = \underline{0} \quad \text{on sideA} \cup \text{sideB}, \tag{14b}$$

$$\underline{u}(\underline{x}, 0) = \underline{0} \quad \text{for all } \underline{x} \in \Omega. \tag{14c}$$

Remark. In this work, we are not explicitly describing the active role of pumps in exchanging ions across the cell membrane. This would require, for example, including in the model the contribution of chemical processes such as ATP consumption. This contribution is implicitly taken into account in our model by means of the ion flux densities $\underline{f}$ that mathematically translate in the boundary conditions the result of these processes.

Simulation results. To ease the interpretation of the reported results, we point out that the Z axis coincides with the axial direction of the pore and it is positively oriented towards the extracellular region. Reported data for the vector-valued variables (such as electric field, current densities, and velocity) are the Z components of the vectors because the other two computed components were comparably negligible. We set $\rho_{\text{fixed}} = 0\,[\text{C m}^{-3}]$, $t_0 = 0\,[\text{s}]$, and $T_{\text{obs}} = 50\,[\text{ns}]$, a sufficiently large value to ensure that the simulated system has reached steady-state conditions at $t = T_{\text{obs}}$.

Remark. In this test case we set to zero the surface charge density in order to single out the influence of each force on model predictions.

The values of the dielectric permittivity of the intrapore water fluid ϵ_f, of the AH fluid shear viscosity μ_f, of the AH fluid mass density ρ_f, and of the diffusion coefficients D_i of each i-th ion species involved in the computational tests are reported in Table 1. All the figures in the remainder of the section illustrate computed results at $t = T_{\text{obs}}$.

model parameter	value	units
ϵ_f	$708.32 \cdot 10^{-10}$	[F cm^{-1}]
μ_f	10^{-2}	[g cm^{-1} s^{-1}]
ρ_f	1	[g cm^{-3}]
D_{K^+}	$1.957 \cdot 10^{-5}$	[cm^2 s^{-1}]
D_{Na^+}	$1.334 \cdot 10^{-5}$	[cm^2 s^{-1}]
D_{Cl^-}	$2.033 \cdot 10^{-5}$	[cm^2 s^{-1}]
$D_{HCO_3^-}$	$1.185 \cdot 10^{-5}$	[cm^2 s^{-1}]
$D_{Ca^{++}}$	$7.92 \cdot 10^{-6}$	[cm^2 s^{-1}]
D_{H^+}	$9.315 \cdot 10^{-5}$	[cm^2 s^{-1}]

Table 1. Values of model parameters.

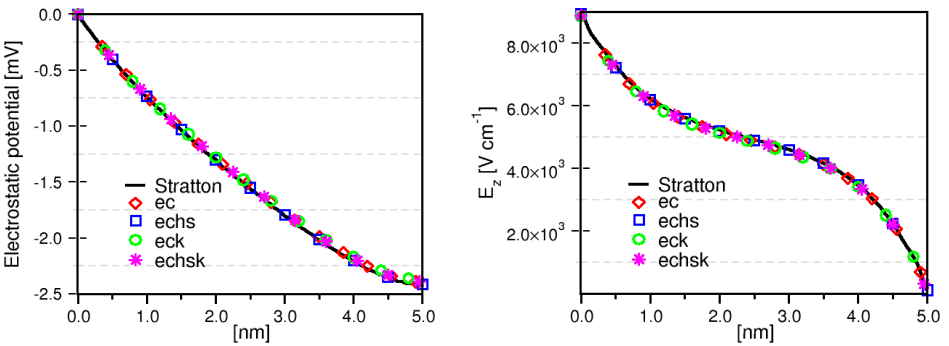

Figure 9. Electric variables along the axis of the pore. Left: electrostatic potential. Right: electric field.

Electric variables. Figure 9 shows the spatial distributions of the electric potential and of the electric field inside the pore. Since no permanent charge is included in the present simulation, the electric potential (and therefore also the electric field) is determined only by the Coulomb interaction among the ions in the pore. This is the reason why electric field and electric potential distributions are scarcely affected by the different models of Section 4. Figure 9, right, also shows that the electric field profile is monotonic inside the pore. This means, on the one hand, that ions are transported with a constant direction depending on their sign (from the intracellular to the extracellular sides in the case of cations, from the extracellular to the intracellular sides in the case of anions) and, on the other hand, that ions cannot be trapped inside the pore; rather they are helped travel throughout the pore. The electrostatic potential shown in Figure 9, left, allows us to perform a *first significant model comparison with experimental data* reported in Table 2 where the measured value of the transepithelial membrane potential $V_m := \varphi(0) - \varphi(L_{\text{ch}})$ is reported for various animals. Results indicate that for all model choices of Section 4, the

V_m [mV]	animal	reference
3.80 ± 0.26	ox	[11]
5.53 ± 0.41	ox	[12]
3.83 ± 0.16	rabbit	[12]
-3.7 ± 0.3	toad	[57]
-1.2 ± 0.1	rabbit	[31]
-1.35 ± 0.08	dog	[22]
$\boxed{-2.5 \pm 0.2}$	monkey	[10]

Table 2. Experimental measurements for the transepithelial membrane potential. The boxed value is the measured data for monkeys and is considered as the reference for comparison with our model simulations.

simulated potential difference is in very good agreement with the data for monkeys [10] which can be considered as the animal species most similar to humans.

Remark. Simulations have been conducted using model parameters taken from human subjects [53]. However, no data are available for transepithelial membrane potential measured in humans, so results were compared to measurements for monkeys because of their physiological and structural similarity to humans.

Remark. The significant variability in the experimental measurements of V_m reported in Table 2 is the result of several factors, possibly depending on the different biophysical structure of the ciliary epithelium in the various animal species (for example, the difference in size and/or ion concentrations in the intra- and extracellular sites), and leads to a different electric equilibrium at steady-state. However, the order of magnitude of all the measured data is in the range of mV, which demonstrates the existence of a common mechanistic framework regulating the formation of the transepithelial membrane potential.

Chemical variables. Figure 10, top, shows the spatial distributions of cations inside the pore whereas Figure 10, bottom, shows the spatial distributions of anions inside the pore. Consistently with the simulated electric field and potential distributions, results indicate that the different models of the volume force density scarcely affect the ion concentrations indicating that the differences in AH fluid velocity, shown in the next section, are not strong enough to modify the ion profiles. As a second comment, we see that the spatial distribution of each ion concentration is not linear inside the pore because of the presence of the electric field that is responsible for the drift contribution in the ion flux constitutive relation (1b). The data reported in Table 3 allow us to perform a *second significant model comparison with experimental data*. The data include the computed value of the axial component of the potassium current density at the extracellular side of the pore $Z = L_{\text{ch}}$ and the computed value of the axial component of the sodium current density at the intracellular side of

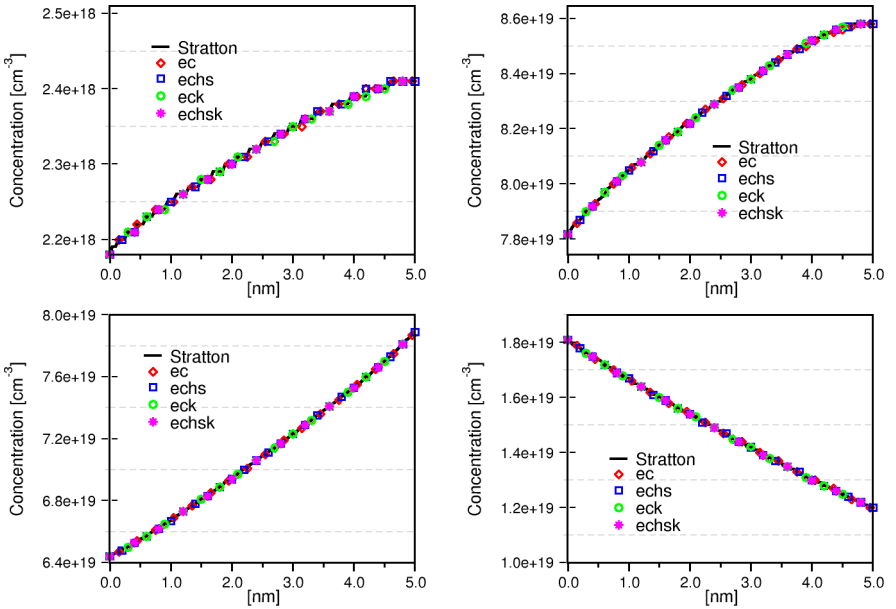

Figure 10. Ion concentration spatial distribution. Top left: K^+. Top right: Na^+. Bottom left: Cl^-. Bottom right: HCO_3^-.

the pore $Z = 0$ for the various choices for the model of the volume force density $\underline{F}_{\text{ion}}$ illustrated in Section 4. To allow a quantitative verification of the biophysical correctness of the predicted exchange of potassium and sodium ions across the pore, we introduce the parameter

$$r := \frac{g_{K^+}}{g_{Na^+}}, \tag{15}$$

where g_{K^+} denotes the boundary value of the flux density of potassium ions that enter into the cell and g_{Na^+} denotes the boundary value of the flux density of sodium ions that flow out of the cell. According to the data of Table 12, we have $r = 2 : 3$. The above parameter expresses the biophysical consistency of the boundary data adopted in the numerical simulation because it coincides with the theoretically expected stoichiometric ratio of the K^+ and Na^+ ions exchanged $(2 : 3)$ by the sodium-potassium pump as represented in the schematic picture of Figure 3. Because of the continuum approach employed in our model, we are going to check the correct functionality of the simulated pump by computing the parameter

$$\mathcal{R} := \left| \frac{J_{Z,K^+}}{J_{Z,Na^+}} \right|, \tag{16}$$

where J_{Z,K^+} is the potassium ion current density at the extracellular side of the pore and J_{Z,Na^+} is the sodium ion current density at the intracellular side of the pore.

model for $\underline{F}_{\text{ion}}$	$J_{Z,\text{K}^+}[\text{Acm}^{-2}]$	$J_{Z,\text{Na}^+}[\text{Acm}^{-2}]$	$\mathcal{R}$
Stratton	−0.064	0.098	0.653
ec	−0.054	0.44	0.123
echs	−0.046	0.74	0.062
eck	−0.064	0.085	0.753
echsk	−0.056	0.38	0.147

Table 3. Computed values of the axial component of the current density for sodium and potassium. The value J_{Z,K^+} is computed at $Z = L_{\text{ch}}$ whereas the value J_{Z,Na^+} is computed at $Z = 0$. We set $\mathcal{R} := |J_{Z,\text{K}^+}/J_{Z,\text{Na}^+}|$. The boxed values indicate the best model predictions to be compared with the theoretical expected ratio 2:3.

Remark. The parameter $\mathcal{R}$ is the counterpart of the quantity r defined in (15) and is quite sensitive to the choice of the volumetric force. The aim of our investigation is to quantify the impact of this choice (if any) on the ion current behavior, as we would like to capture the physiological function of the pumps/exchangers. The correct predicted ratio, moreover, does not only ensure the expected physiological effect, but also confirms the self-consistency of the model, which is not guaranteed a priori for every volume force density model.

As a first comment, the results of Table 3 show that for each considered model of $\underline{F}_{\text{ion}}$ the computed potassium current density is negative whereas the computed sodium current density is positive. This is consistent with the physiological function of the sodium-potassium pump because sodium ions flow out of the cell and potassium ions flow into the cell. As a second comment, the computed values of $\mathcal{R}$ indicate that agreement with the theoretical expected ratio $2:3$ is achieved only in the case of the Stratton model and of the eck model, whereas the values of $\mathcal{R}$ computed with the other models are not in a feasible range. This allows us to conclude that the VE-PNP model predicts a correct direction of ion flow for the sodium-potassium pump in a good quantitative agreement with the stoichiometric ratio of the pump only if the *Stratton* or the *eck* model is adopted to mathematically represent the volume force density in the linear momentum balance equation for the aqueous intracellular fluid.

Remark. This outcome is physically significant considering the fact that imposing on two different boundaries the ratio of the ion currents is no guarantee that such a ratio will be respected in the interior of the three-dimensional channel domain, whereas the value $\mathcal{R}$ is reached only at steady-state.

AH fluid variables. Figure 11 shows the spatial distributions of the component of the AH fluid velocity and of the volumetric force density along the Z axis. Predicted velocities are all negative except in the case of the eck model; similarly, the computed volumetric force densities are all positive except in the case of the

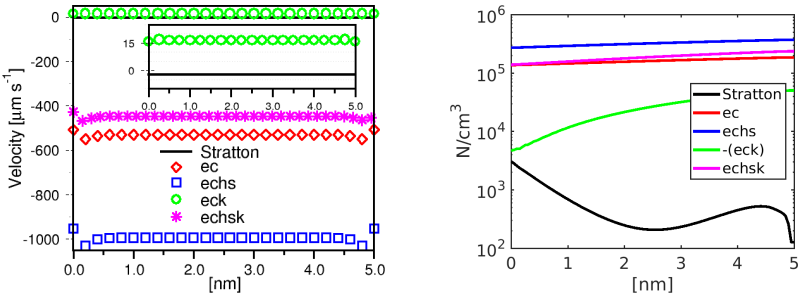

Figure 11. AH fluid variables along the axis of the pore. Left: aqueous humor fluid velocity. Right: volumetric force density.

model for $\underline{F}_{\text{ion}}$	$\bar{v}_Z[\mu\text{m s}^{-1}]$
Stratton	-2.34
ec	-529.5
echs	-992
eck	$\boxed{16.54}$
echsk	-445.6

Table 4. Computed mean values of the axial component of the intrapore AH fluid velocity. The boxed value indicates the sole model results that are in agreement with an outflux of aqueous humor from the cell into the extracellular side.

eck model (in Figure 11, right, we have reported the absolute value of the force density). Moreover, it is easy to check that the variation of the velocity is one-to-one correlated with the variation of the volumetric force density because of the homogeneous initial and boundary conditions that are applied to the Stokes system.

Table 4 reports the values of the AH fluid velocity computed at the center of the pore for each model considered in Section 4. Results allow us to perform a *third significant model comparison with experimental data*: only by describing the volume force density through the *eck* model is the VE-PNP formulation able to predict a positive AH fluid velocity which corresponds to the production of AH from the cell into the basolateral space. More specifically, if we assume a value of $2.5\,[\mu\text{l s}^{-1}]$ for a normal AH flow through the eye pupil [36] and an equivalent radius of 1 [mm] for the eye pupil of an adult, we see that a physiological value of v_Z is of about $14\,[\mu\text{m s}^{-1}]$, which agrees well with the value of $16.54\,[\mu\text{m s}^{-1}]$ predicted by the eck model. The other results from Table 4 (negative velocities) indicate that the magnitude of the predicted AH flow is nonphysically large, except in the case of the Stratton model, thus justifying its wide adoption in the literature.

Conclusions. The study of the interaction between the ion component (Na^+-K^+ pump) and AH production through a mathematical continuum approach based on

the VE-PNP model, under the condition of adopting the *eck* formulation of the volume force density that constitutes the source term in the fluid momentum balance equation, shows that simulation results are in agreement with

(1) the experimentally measured value of transepithelial membrane potential,

(2) the physiological stoichiometric rate of 2 : 3 that characterizes the sodium-potassium pump,

(3) the direction of current densities of sodium (flowing out of the cell) and potassium (flowing into the cell),

(4) the direction of AH flow (outward the cell), and

(5) the magnitude of AH fluid velocity.

The aforementioned results support the mathematical and biophysical motivation to adopt the *eck* model in the remainder of the article where we introduce a more realistic geometrical description of the ion pore and we include the main ion pumps and exchangers to describe the electric pressure exerted by the ions on the intrapore AH fluid.

7. Cellular scale simulation of ion pumps and exchangers in AH production

In this section we use the VE-PNP model to carry out an extensive quantitative investigation on the active role of the ion exchanges that are identified in [30; 29] as important determinants in AH secretion. To this purpose, we adopt the VE-PNP formulation in which the volumetric force exerted from ions onto the fluid is described by the eck model illustrated in Section 4. In addition, we employ in the numerical simulations a more realistic ion pore geometry than that shown in Figure 8, obtained by including in the computational domain a small amount of cell membrane as well as the presence of the antichambers.

Remark. We emphasize that only the Poisson equation (1c) is solved in the large rectilinear domain (represented in gray color in Figure 12). The dimensions of this domain are set in such a way that boundary effects have no influence on the solution computed in the pore domain.

The unified modeling and computational framework is here applied to study the function of each ion pump and exchanger illustrated in Section 2 with the goal of examining the output results, such as electrostatic potential, stoichiometric ratios, and AH velocity, as functions of the input parameters, such as the osmotic coefficient, the value of the permanent electric charge density, and the nonhomogeneous Neumann boundary conditions for ion flux densities.

Figure 12 shows the geometrical structure constituting the computational domain. The parallelepiped containing the cylinder represents the regions in which the

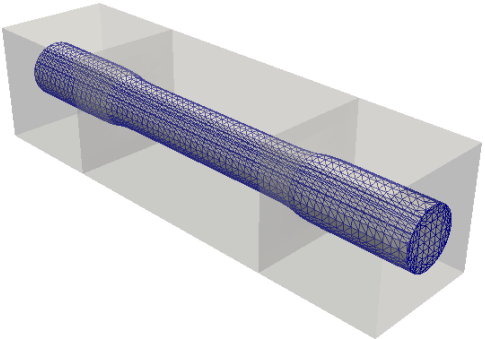

Figure 12. Computational domain for the simulation of the ion pumps and exchangers involved in AH production. The two external cylinders represent the pore antichambers whereas the central cylinder is the pore region. The partition of the pore domain into about 110391 tetrahedral elements is illustrated, whereas the mesh partition of the region surrounding the pore is not shown for visual clarity.

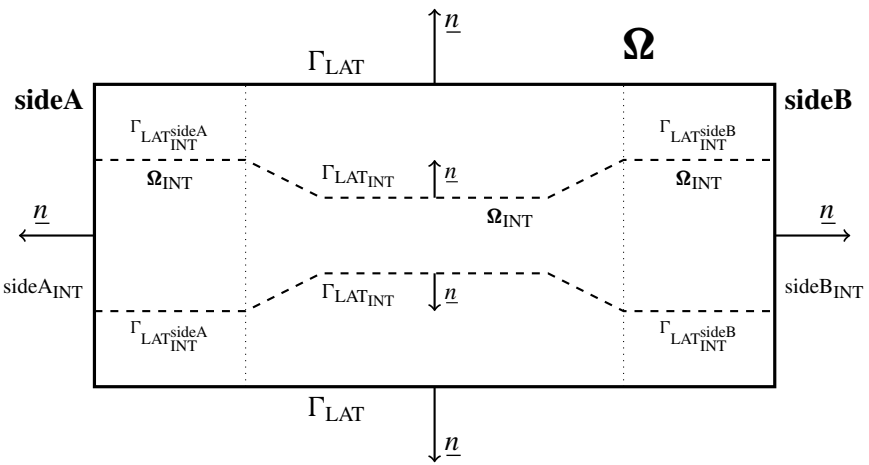

Figure 13. Two-dimensional cross-section of the pore geometry and boundary labels for the simulation of AH production.

transmembrane pore is divided, namely two external cylinders representing the pore antichambers and a central cylinder representing the ion pore. The parallelepiped is composed by the union of two cubes of side equal to 2.5 [nm] and by a central parallelepiped of length equal to 5 [nm] in such a way that the total length is equal to 10 [nm]. The portion of the cylindrical structure inside the two external cubes has a radius of 0.6 [nm] whereas the portion inside the central parallelepiped has a radius of 0.4 [nm]. The adopted geometrical representation is based on the biophysical setting analyzed in [9; 8] and aims at reproducing the morphology of a realistic protein membrane pore, where the two external cylinders play the role of pore

antichambers and the cylinder at the center plays the role of the pore region in which the main electrochemical and fluid processes take place. The full domain has been partitioned in tetrahedra as reported in Figure 12 where the discretization of the parallelepiped surrounding the cylinder is not shown for sake of visual clarity. Referring to the notation of Figure 13, in the remainder of the section, the VE-PNP equations (1a)–(1b) and the Stokes system (1e)–(1h) are solved only inside the cylinder Ω_{INT} whereas the Poisson equation (1c)–(1d) is solved in the whole domain Ω.

Boundary and initial conditions. In Section 6 we have highlighted the fundamental role played by the BCs in the simulation of the sodium-potassium pump. Because here we are treating a wider variety of ion exchangers and we have a more complex computational domain as well as the presence of a larger number of ion species, to help the clarity of the discussion we report in Figure 13 a two-dimensional cross-section of the pore geometry and identify the various regions of the domain with the corresponding labels for further reference.

Poisson equation. Because of the presence of the interface between the internal cylinder and the surrounding parallelepiped, we need to treat the jump of the electric displacement across that interface as well as the possible presence of electric charge on this interface. Let $\gamma := \Gamma_{\text{LAT}_{\text{INT}}^{\text{sideA}}} \cup \Gamma_{\text{LAT}_{\text{INT}}^{\text{sideB}}} \cup \Gamma_{\text{LAT}_{\text{INT}}}$ denote the two-dimensional surface separating the pore region from the surrounding membrane region as depicted in Figure 13. For a given vector-valued function $\underline{\tau} : \Omega \to \mathbb{R}^3$ we define the jump of $\underline{\tau}$ across the surface γ as

$$[\![\underline{\tau}]\!]_\gamma := (\underline{\tau}|_{\Omega\setminus\Omega_{\text{INT}}}|_\gamma - \underline{\tau}|_{\Omega_{\text{INT}}}|_\gamma) \cdot \underline{n},$$

whereas for a given scalar-valued function $\phi : \Omega \to \mathbb{R}$ we define the jump of ϕ across the surface γ as

$$[\![\phi]\!]_\gamma := \phi|_{\Omega\setminus\Omega_{\text{INT}}}|_\gamma \underline{n} - \phi|_{\Omega_{\text{INT}}}|_\gamma \underline{n}.$$

We notice that the jump of a vector-valued function is a scalar function whereas the jump of a scalar-valued function is a vector function. For all $t \in I_T$, the BCs for the Poisson equation (1c)–(1d) are

$$\varphi = 0 \quad \text{on sideA}_{\text{int}}, \tag{17a}$$

$$\underline{D} \cdot \underline{n} = 0 \quad \text{on } \Gamma_{\text{LAT}} \cup \text{sideB} \cup \text{sideA} \cup \text{sideB}_{\text{int}}, \tag{17b}$$

$$[\![\underline{D}]\!]_\gamma = h_\gamma \quad \text{on } \gamma, \tag{17c}$$

$$[\![\varphi]\!]_\gamma = 0 \quad \text{on } \gamma, \tag{17d}$$

where

$$h_\gamma = \begin{cases} \sigma_{\text{fixed}} & \text{on } \Gamma_{\text{LAT}_{\text{INT}}}, \\ 0 & \text{on } \Gamma_{\text{LAT}_{\text{INT}}^{\text{sideA}}} \cup \Gamma_{\text{LAT}_{\text{INT}}^{\text{sideB}}}, \end{cases}$$

pump/exchanger	σ_{fixed} [C cm^{-2}]
sodium-potassium pump	$-1 \cdot 10^{10}$
calcium-sodium exchanger	$-1.2 \cdot 10^{12}$
chloride-bicarbonate exchanger	$+3.9 \cdot 10^{11}$
sodium-proton exchanger	$-2.65 \cdot 10^{12}$

Table 5. Values of the fixed charge density σ_{fixed}.

$\text{Na}^+ = \text{Na}^+_{\text{in}}$	$\underline{f}_{\text{K}^+} \cdot \underline{n} = g_{\text{K}^+}$	on sideA_{int}
$\text{K}^+ = \text{K}^+_{\text{out}}$	$\underline{f}_{\text{Na}^+} \cdot \underline{n} = g_{\text{Na}^+}$	on sideB_{int}
$\underline{f}_{\text{Na}^+} \cdot \underline{n} = 0$	$\underline{f}_{\text{K}^+} \cdot \underline{n} = 0$	on γ
$\text{K}^{+^0}(x) = \text{K}^+_0$	$\text{Na}^{+^0}(x) = \text{Na}^+_0$	in Ω_{INT}
$\text{Cl}^- = \text{Cl}^-_{\text{in}}$	$\text{HCO}_3^- = \text{HCO}_{3_{\text{in}}}^-$	on sideA_{int}
$\text{Cl}^- = \text{Cl}^-_{\text{out}}$	$\text{HCO}_3^- = \text{HCO}_{3_{\text{out}}}^-$	on sideB_{int}
$\underline{f}_{\text{Cl}^-} \cdot \underline{n} = 0$	$\underline{f}_{\text{HCO}_3^-} \cdot \underline{n} = 0$	on γ
$\text{Cl}^{-^0}(x) = \text{Cl}^-_0$	$\text{HCO}_3^{-^0}(x) = \text{HCO}_{3_0}^-$	in Ω_{INT}

Table 6. BCs and ICs for the sodium-potassium pump.

σ_{fixed} [C m^{-2}] being a given distribution of superficial permanent charge density that mathematically represents the electric charge contained in the amino-acid structure of the protein surrounding the ion pore. We notice that the interface condition (17d) expresses the physical fact that the electric potential is a continuous function across γ, whereas the interface condition (17c) expresses the physical fact that the normal component of the displacement vector is discontinuous across the surface separating the pore region and the lipid membrane bilayer because of the presence of amino-acid fixed charge density σ_{fixed}. The value of σ_{fixed} needs be determined in order to reproduce the correct functionality of the several ion pumps/exchangers. To this purpose, a simulation campaign has to be performed to heuristically tune-up the values of σ_{fixed} (see [45] for the sodium-potassium pump). The results of this procedure in the present context are reported in Table 5.

Nernst–Planck equations. The several ion pumps/exchangers involved in AH production are simulated by considering the contribution of different ions in order to produce the correct electrostatic potential drop across the cell membrane. The list of these ions is reported below. In complete analogy with what was done in Section 6 for the BCs and ICs of the Nernst–Planck equations (1a)–(1b), we report in Tables 6–9 the BCs and ICs adopted to reproduce the correct biophysical functionality of each ion pump/exchanger:

$K^+ = K^+_{in}$	$Na^+ = Na^+_{in}$	$\underline{f}_{Ca^{++}} \cdot \underline{n} = g_{Ca^{++}}$	on $sideA_{int}$
$K^+ = K^+_{out}$	$Ca^{++} = Ca^{++}_{out}$	$\underline{f}_{Na^+} \cdot \underline{n} = g_{Na^+}$	on $sideB_{int}$
$\underline{f}_{Ca^{++}} \cdot \underline{n} = 0$	$\underline{f}_{Na^+} \cdot \underline{n} = 0$	$\underline{f}_{K^+} \cdot \underline{n} = 0$	on γ
$K^{+^0}(x) = K^+_0$	$Na^{+^0}(x) = Na^+_0$	$Ca^{++^0}(x) = Ca^{++}_0$	in Ω_{INT}
$Cl^- = Cl^-_{in}$	$HCO_3^- = HCO_{3_{in}}^-$		on $sideA_{int}$
$Cl^- = Cl^-_{out}$	$HCO_3^- = HCO_{3_{out}}^-$		on $sideB_{int}$
$\underline{f}_{Cl^-} \cdot \underline{n} = 0$	$\underline{f}_{HCO_3^-} \cdot \underline{n} = 0$		on γ
$Cl^{-^0}(x) = Cl^-_0$	$HCO_3^{-^0}(x) = HCO_{3_0}^-$		in Ω_{INT}

Table 7. BCs and ICs for the calcium-sodium exchanger.

$K^+ = K^+_{in}$	$Na^+ = Na^+_{in}$	on $sideA_{int}$
$K^+ = K^+_{out}$	$Na^+ = Na^+_{out}$	on $sideB_{int}$
$\underline{f}_{Na^+} \cdot \underline{n} = 0$	$\underline{f}_{K^+} \cdot \underline{n} = 0$	on γ
$K^{+^0}(x) = K^+_0$	$Na^{+^0}(x) = Na^+_0$	in Ω_{INT}
$\underline{f}_{Cl^-} \cdot \underline{n} = g_{Cl^-}$	$\underline{f}_{HCO_3^-} \cdot \underline{n} = g_{HCO_3^-}$	on $sideA_{int}$
$Cl^- = Cl^-_{out}$	$HCO_3^- = HCO_{3_{out}}^-$	on $sideB_{int}$
$\underline{f}_{Cl^-} \cdot \underline{n} = 0$	$\underline{f}_{HCO_3^-} \cdot \underline{n} = 0$	on γ
$Cl^{-^0}(x) = Cl^-_0$	$HCO_3^{-^0}(x) = HCO_{3_0}^-$	in Ω_{INT}

Table 8. BCs and ICs for the chloride-bicarbonate exchanger.

Na^+-K^+ pump. Na^+, K^+, Cl^-, and HCO_3^- are included.

Ca^{++}-Na^+ exchanger. Na^+, K^+, Cl^-, HCO_3^-, and Ca^{++} are included.

Cl^--HCO_3^- exchanger. Na^+, K^+, Cl^-, and HCO_3^- are included.

Na^+-H^+ exchanger. Na^+, K^+, Cl^-, HCO_3^-, and H^+ are included.

The values of the boundary data for the ion pumps and exchangers are specified in Tables 14–17.

Stokes system. We adopt the same BCs and ICs as in Section 6:

$$\underline{u} = \underline{0} \quad \text{on } \gamma, \tag{18a}$$

$$\underline{\underline{\sigma}}\,\underline{n} = \underline{0} \quad \text{on } sideA_{int} \cup sideB_{int}, \tag{18b}$$

$$\underline{u}(\underline{x}, 0) = \underline{0} \quad \text{for all } \underline{x} \in \Omega_{INT}. \tag{18c}$$

As already pointed out, to describe the volumetric force on the right-hand side of the linear momentum balance equation in the Stokes system, we use the *eck*

$K^+ = K^+_{in}$	$Na^+ = Na^+_{in}$	$\underline{f}_{H^+} \cdot \underline{n} = g_{H^+}$	on sideA_{int}
$K^+ = K^+_{out}$	$H^+ = H^+_{out}$	$\underline{f}_{Na^+} \cdot \underline{n} = g_{Na^+}$	on sideB_{int}
$\underline{f}_{H^+} \cdot \underline{n} = 0$	$\underline{f}_{Na^+} \cdot \underline{n} = 0$	$\underline{f}_{K^+} \cdot \underline{n} = 0$	on γ
$K^{+^0}(x) = K^+_0$	$Na^{+^0}(x) = Na^+_0$	$H^{+^0}(x) = H^+_0$	in Ω_{INT}
$Cl^- = Cl^-_{in}$	$HCO_3^- = HCO^-_{3_{in}}$		on sideA_{int}
$Cl^- = Cl^-_{out}$	$HCO_3^- = HCO^-_{3_{out}}$		on sideB_{int}
$\underline{f}_{Cl^-} \cdot \underline{n} = 0$	$\underline{f}_{HCO_3^-} \cdot \underline{n} = 0$		on γ
$Cl^{-^0}(x) = Cl^-_0$	$HCO_3^{-^0}(x) = HCO^-_{3_0}$		in Ω_{INT}

Table 9. BCs and ICs for the sodium-proton exchanger.

Pump/exchanger	k [N m]
sodium-potassium pump	$4.1 \cdot 10^{-19}$
calcium-sodium exchanger	$24 \cdot 10^{-19}$
chloride-bicarbonate exchanger	$4.1 \cdot 10^{-19}$
sodium-proton exchanger	$4 \cdot 10^{-19}$

Table 10. Values of the electrochemical osmotic parameter k for each pump/exchanger involved in the process of AH production.

model. The value of k is considered a characteristic property of the single pump and exchanger, and it is reported in Table 10.

Simulation results. Reported data for the vector-valued variables (such as electric field, current densities, and AH fluid velocity) are the Z component of the vectors because the other two computed components were comparably negligible. We set $t_0 = 0$ [s] and $T_{obs} = 50$ [ns], a sufficiently large value to ensure that the simulated system has reached steady-state conditions at $t = T_{obs}$: all the figures in the remainder of the section illustrate computed results at this time. The values of the dielectric permittivity of the intrapore fluid ϵ_f, of the AH fluid shear viscosity μ_f, of the AH fluid mass density ρ_f, and of the diffusion coefficients D_i of each i-th ion species involved in the computational tests are reported in Table 1.

Electric variables. Figure 14, left, shows the transepithelial electrostatic potential as calculated by the simulations. We note how the electric potential is strongly influenced by the presence of the fixed surface charge density σ_{fixed} in the central region of the domain (see Table 5), with particular emphasis on the case of the sodium-proton exchanger. It is remarkable to notice that, as in the case of the simulation of the sodium-potassium pump illustrated in Section 6, also in this more complex biophysical setting, for each simulated exchanger, the computed

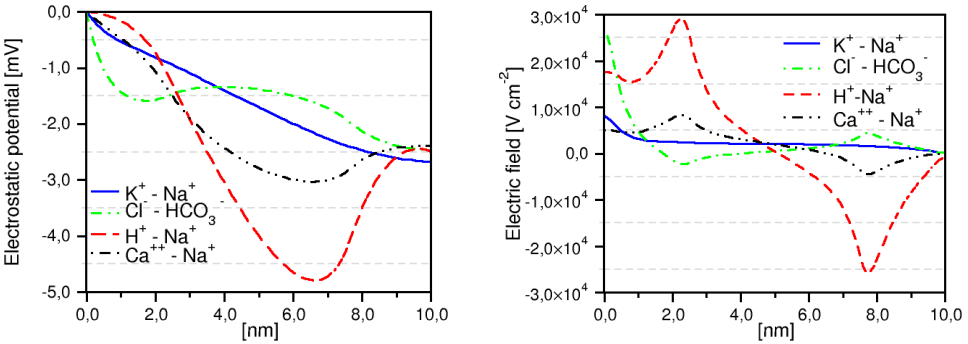

Figure 14. Electric variables along the axis of the pore. Left: electrostatic potential. Right: electric field.

value of *the transepithelial membrane potential is in very good agreement with the experimental data* for monkeys reported in Table 2.

Figure 14, right, shows the computed spatial behavior of the axial component E_Z of the electric field for each considered pump/exchanger. Consistently with electrostatic potential, we see that in all simulations E_Z is a monotonic function of position in the central region of the pore. Then, coming closer to the outlet section at $Z = L_{\text{ch}}$, all the simulated profiles become flat in accordance with the homogeneous Neumann boundary condition (17b). Specifically, in the case of cation pump/exchanger, the electric field is decreasing along the central part of the pore whereas in the case of the chloride-bicarbonate exchanger the electric field is increasing. These two opposite behaviors are related to the presence of surface charge on $\Gamma_{\text{LAT}_{\text{INT}}}$ of opposite sign (negative for cation pumps/exchangers, positive for the anion exchanger). In the case of the sodium-proton exchanger, the electric field profile experiences a large increase in magnitude moving along the pore axis from the intracellular side towards the extracellular side because of the elevated negative fixed charge density distributed on the lateral surface on the pore region (see Table 5).

Chemical variables. The computed profiles of the ion concentrations for each simulated ion pump and exchanger are reported in Figure 15. Results show the onset of a concentration gradient for each simulated ion species which appears not to be spatially constant for all ion species because of the action of the electric drift force which displaces the ion profile from the linear equilibrium distribution corresponding to a null electric field. Particularly worth noticing is the occurrence of significant variations for the concentration of the sodium ion in the simulation of the sodium-proton exchanger shown in Figure 15, bottom right. These variations are the result of the attractive electrostatic force exerted on the sodium ions by the elevated negative fixed charge density distributed on the lateral surface on the pore region (see Table 5).

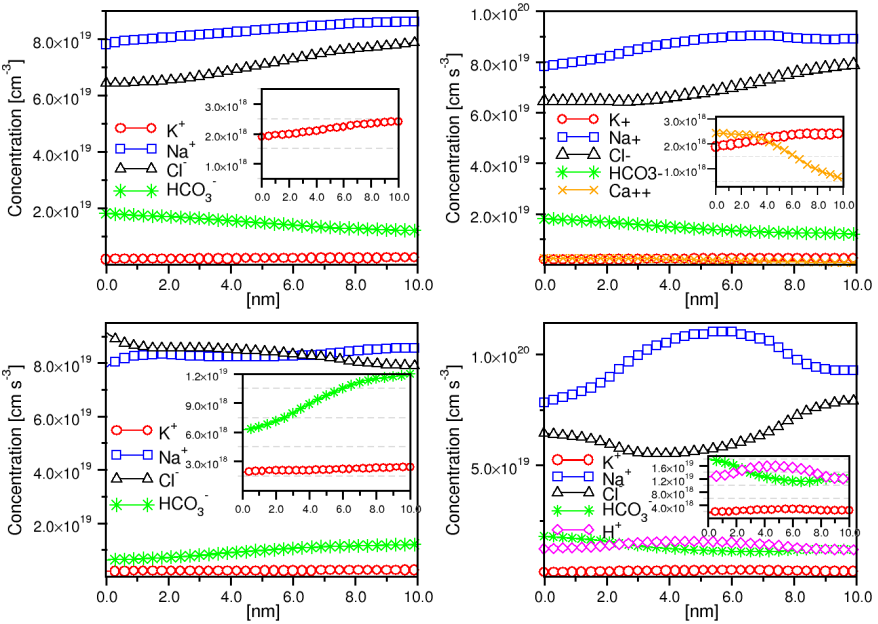

Figure 15. Computed ion concentration along the Z axis. Top left: sodium-potassium pump. Top right: calcium-sodium exchanger. Bottom left: chloride-bicarbonate exchanger. Bottom right: sodium-proton exchanger.

Figure 16 shows the spatial distributions of the computed axial component of the ion current density for each pump and exchanger. For sake of clarity, in these figures we report only the current density related to the pump/exchanger functionality. We notice that for each ion, the value of the current density along the Z axis is not constant because the cross-section varies along the pore axis.

First, the sign of the computed current density for each simulated pump/exchanger agrees with the theoretically expected direction. As a second comment, *the predicted value of the stoichiometric ratio $\mathcal{R}$ reasonably agrees with the corresponding theoretical value r*. Specifically, in the case of the sodium-potassium pump shown in Figure 16, top left, $\mathcal{R} = 0.83$ whereas $r = 2:3 = 0.67$, in the case of the calcium-sodium exchanger shown in Figure 16, top right, $\mathcal{R} = 0.43$ whereas $r = 1:3 = 0.33$, in the case of the chloride-bicarbonate exchanger shown in Figure 16, bottom left, we have $\mathcal{R} = 1.23$ to be compared with $r = 1:1$, and in the case of the sodium-proton exchanger shown in Figure 16, bottom right, the value $\mathcal{R} = 0.92$ agrees fairly well with the theoretical value $r = 1:1$.

AH fluid variables. Figure 17 shows the spatial distribution of the axial component of the intrapore AH fluid velocity predicted by the simulation with the VE-PNP model of each ion pump and exchanger involved in the process of AH production. Results exhibit a significant difference among the various pumps/exchangers mainly

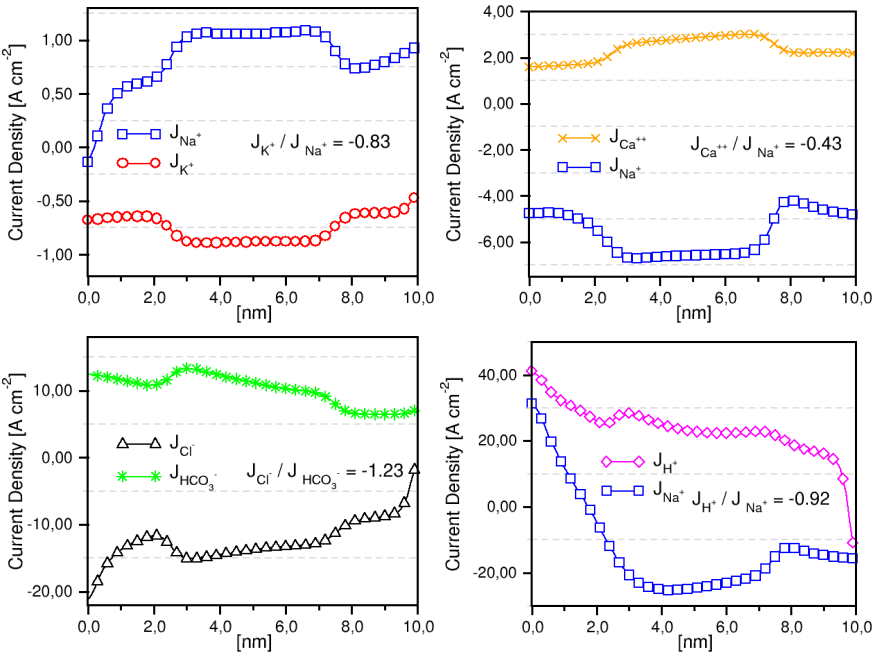

Figure 16. Computed ion current density along the Z axis. Top left: sodium-potassium pump. Top right: calcium-sodium exchanger. Bottom left: chloride-bicarbonate exchanger. Bottom right: sodium-proton exchanger.

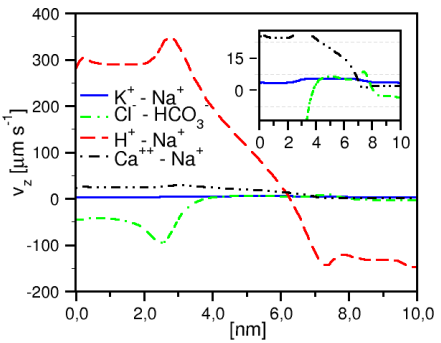

Figure 17. Computed spatial distribution of the axial component of AH fluid velocity for each pump/exchanger involved in AH production.

due to the presence of the fixed surface charge density σ_{fixed} in the central region of the domain that needed to be included to reproduce the correct pump functionalities. Specifically, in the case of the cation-based ion pumps/exchangers, model simulation predicts a positive value of the AH velocity in the whole computational domain whereas in the case of the chloride-bicarbonate exchanger the computed AH fluid velocity is strictly positive only in the central region of the domain. In the case of

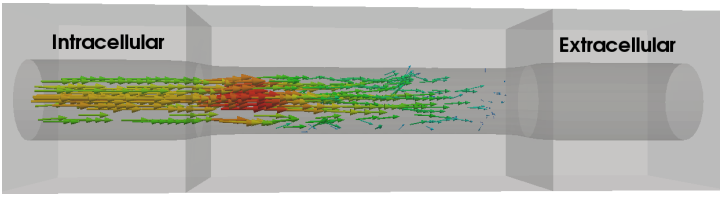

Figure 18. Computed three-dimensional spatial distribution of AH fluid velocity in the case of the calcium-sodium exchanger.

the sodium-proton exchanger, the elevated fixed surface charge density on $\Gamma_{\mathrm{LAT_{INT}}}$ gives rise to a change of sign of the axial component of the electric field at about the center of the domain. This, in turn, gives rise to a change of sign in the volume force density $\underline{F}_{\mathrm{ion}}$ in the momentum balance equation of the AH fluid, causing an inversion of the intrapore AH fluid flow at $Z = 7.5\,[\mathrm{nm}]$ where the direction of the axial velocity changes sign, from positive to negative. These results seem to suggest that the main ion pumps/exchangers contributing to AH secretion are those that actively involve Na^+.

Figure 18 shows an example of three-dimensional computed spatial distribution of the AH fluid velocity in the case of the calcium-sodium exchanger. Results clearly show that AH flows from the intracellular space towards the extracellular space.

Further remarks on pump/exchanger functionality. In this section we briefly address a series of further considerations on the analysis of the simulation of the various ion pumps and exchangers involved in the process of AH production, in particular, those related to pump/exchanger functionality. The first consideration concerns the temporal evolution of calcium in the Ca^{++}-Na^+ exchanger. To this purpose, Figure 19, top left, illustrates the spatial calcium concentration at $t = 0$ (dashed line) and that at $t = T_{\mathrm{obs}}$ (solid line). Results show a decrease of the level of calcium in the intracellular side of the domain.

Remark. This result is interesting from a physiological viewpoint due to the fact that the intracellular initial concentration of Ca^{++} is imposed at $3.011 \cdot 10^{18}\,\mathrm{cm}^{-3} = 5\,\mathrm{mM}$, which corresponds to a pathological condition of calcium excess within the cell [2; 14]. Such a decrease is slow because of the relatively low value $D_{Ca^{++}} = 7.92 \cdot 10^{-6}\,[\mathrm{cm}^2\,\mathrm{s}^{-1}]$ of the diffusion coefficient adopted in the numerical simulation, but nonetheless, it is compatible with a theoretical expectation of a value of $10^{-4}\,\mathrm{mM}$ for healthy intracellular calcium level [2; 14].

The second consideration concerns the time behavior of carbonate (HCO_3^-) in the chloride-bicarbonate exchanger. To this purpose, Figure 19, top right, illustrates the spatial bicarbonate concentration at $t = 0$ (dashed line) and that at $t = T_{\mathrm{obs}}$

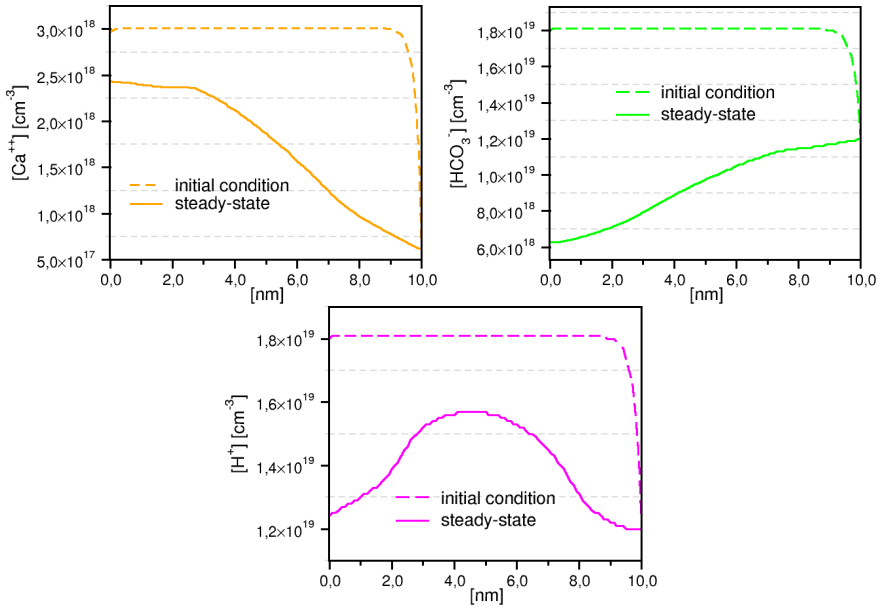

Figure 19. Computed ion current density along the Z axis at various times. Dashed line: distribution at $t = 0$. Solid line: distribution at $t = T_{\text{obs}}$. Top left: $[Ca^{++}]$ in the calcium-sodium exchanger. Top right: $[HCO_3^-]$ for the chloride-bicarbonate exchanger. Bottom: $[H^+]$ for the sodium-proton exchanger.

(solid line). Results show a significant decrease of the level of bicarbonate in the intracellular region. This behavior agrees with the fact that the simulated electric field profile for the chloride-bicarbonate exchanger is positive in the intracellular region of the domain (see Figure 14, right) and therefore bicarbonate ions are swept away from left to right. For further analysis of the importance of the bicarbonate ion in AH production, we refer to [35].

The third consideration concerns the spatial distribution of the proton (H^+) in the simulation of the sodium-proton exchanger. To this purpose, Figure 19, bottom, illustrates the spatial proton profile at $t = 0$ (dashed line) and that at $t = T_{\text{obs}}$ (solid line). Similarly to the previous case of carbonate, results show a significant reduction with simulation time of proton concentration in all the domain. However, unlike the previous case, concentration reduction equally occurs in both intracellular and extracellular sides whereas proton accumulation occurs in the pore region. This behavior is due to the direction of the electric field (see Figure 14, right) which pushes H^+ from left to right in the intracellular side (where $E_Z > 0$) and from right to left in the extracellular side (where $E_Z < 0$).

Summary of the simulation results. In Table 11 we report the main outcomes of the simulation of ion pumps and exchangers carried out in the context of AH

Pump/exchanger	k [N cm]	σ_{fixed} [C cm^{-2}]	φ_m [mV]	$\mathcal{R}$	v_Z [μm s^{-1}]
K^+-Na^+	$4.1 \cdot 10^{-19}$	$-1.0 \cdot 10^{10}$	-2.67	0.83 (0.67)	[4, 5.56]
Cl^--HCO_3^-	$24 \cdot 10^{-19}$	$+3.9 \cdot 10^{11}$	-2.46	1.23 (1)	[-100, $+6.56$]
Na^+-H^+	$4.0 \cdot 10^{-19}$	$-2.65 \cdot 10^{12}$	-2.49	0.92 (1)	[-150, 300]
Ca^{++}-Na^+	$3.95 \cdot 10^{-19}$	$-6 \cdot 10^{11}$	-2.39	0.43 (0.33)	[2, 28]

Table 11. A summary of the simulation results for ion pumps and exchangers involved in AH production. Aside the predicted value of $\mathcal{R}$ we report in parentheses the theoretically expected value. The column v_Z reports for each row the predicted range of the AH fluid velocity.

secretion induced at the cellular scale level by the effect of ion pressure exerted on transmembrane fluid. To summarize, *a unified modeling and computational framework allowed us to successfully simulate the functionality of several ion pump/exchangers* while preserving at the same time the features of each single pump/exchanger, by a proper selection of the ion flux density BCs, of the osmotic gradient coefficient, and of the amount of amino-acid charge in the pore protein folder. These conclusions are significant outcomes of our computational model because osmotic gradient coefficient and permanent electric surface charge do not yet have a quantitative comparison with experimental data, though they have been shown to be essential parts of the biophysical description of the pore and to play a relevant role in determining AH flow direction.

8. Conclusions, model limitations, and future objectives

A unified modeling and computational framework with electrochemical osmotic correction and with a realistic geometry to represent the computational domain has been proposed to investigate the main functional principles of the sodium-potassium pump and the calcium-sodium, chloride-bicarbonate, and sodium-proton exchangers that are involved in the production of aqueous humor in the ciliary body of the eye.

The theoretical model has been demonstrated to correctly reproduce, for each simulated ion pump and exchanger, existing experimental data of transepithelial membrane potential in animal models. The model has also allowed, for the first time to the best of our knowledge in the study of AH production, the quantitative analysis of novel biophysical mechanisms such as the physiological stoichiometric rate, the direction of AH flow, and the magnitude of AH fluid velocity. Thus, the present study motivates the further development of this modeling approach to (i) simulate the simultaneous presence and action of the several ion pump/exchangers considered in this work, with the aim of quantitatively estimating their reciprocal influence, (ii) include the presence of other molecules actively transported through the cell membrane, including ascorbic acid, which is secreted by a transporter

(sodium-dependent vitamin C transporter 2 (SVCT2)) [55], and (iii) the simulation of the effect of administration of a drug in the regulation of AH secretion.

It is expected that such theoretical advancement of the frontier of knowledge in this branch of human sciences may significantly help design new molecules for drug synthesis and, as a consequence, considerably reduce time and costs for clinical availability of new pharmacological therapies.

It is important to emphasize, though, that a number of biophysical limitations still affect the proposed mathematical model of aqueous humor dynamics. Among them, we mention that our model does not account for (i) autonomic system pathways, specifically the sympathetic and parasympathetic pathways [54], (ii) variations due to the circadian rhythm [50], which would require a higher-order temporal discretization in order to account for the temporal transients, or (iii) the role of aquaporins in the exchange of fluid across the cell membrane [46]. A research effort to address these limitations is currently in progress.

Acknowledgements

PhD candidate Sala is supported by a scholarship of the Ministère de l'Enseignement supérieur et de la Recherche (France). Doctor Sacco has been partially supported by Micron Semiconductor Italia S.r.l., SOW number 4505462139. Doctor Guidoboni has been partially supported by the awards NSF DMS-1224195 and NSF DMS-1853222, the Chair Gutenberg funds of the Cercle Gutenberg (France), and the LabEx IRMIA (University of Strasbourg, France). Doctor Harris has been partially supported by Research to Prevent Blindness (New York) and the award NSF DMS-1853303.

Data tables

K_0^+ $2.41 \cdot 10^{18}$ [cm^{-3}]	g_{K^+} $+4 \cdot 10^{17}$ [cm^{-2}s^{-1}]	K_{out}^+ $2.41 \cdot 10^{18}$ [cm^{-3}]
Na_0^+ $8.19 \cdot 10^{19}$ [cm^{-3}]	Na_{in}^+ $7.82 \cdot 10^{19}$ [cm^{-3}]	g_{Na^+} $+6 \cdot 10^{17}$ [cm^{-2}s^{-1}]

Table 12. Boundary and initial data for the cations in Section 6.

Cl_0^- $7.17 \cdot 10^{19}$ [cm^{-3}]	Cl_{in}^- $6.44 \cdot 10^{19}$ [cm^{-3}]	Cl_{out}^- $7.89 \cdot 10^{19}$ [cm^{-3}]
$HCO_{3,0}^-$ $1.51 \cdot 10^{19}$ [cm^{-3}]	$HCO_{3,in}^-$ $1.81 \cdot 10^{19}$ [cm^{-3}]	$HCO_{3,out}^-$ $1.2 \cdot 10^{19}$ [cm^{-3}]

Table 13. Boundary and initial data for the anions in Section 6.

K_0^+ [cm^{-3}] $2.41 \cdot 10^{18}$	g_{K^+} [cm^{-2}s^{-1}] $+4 \cdot 10^{19}$	K_{out}^+ [cm^{-3}] $2.41 \cdot 10^{18}$
Na_0^+ [cm^{-3}] $8.19 \cdot 10^{19}$	Na_{in}^+ [cm^{-3}] $7.82 \cdot 10^{19}$	g_{Na^+} [cm^{-2}s^{-1}] $+6 \cdot 10^{19}$
Cl_0^- [cm^{-3}] $7.17 \cdot 10^{19}$	Cl_{in}^- [cm^{-3}] $6.44 \cdot 10^{19}$	Cl_{out}^- [cm^{-3}] $7.89 \cdot 10^{19}$
$HCO_{3\,0}^-$ [cm^{-3}] $1.51 \cdot 10^{19}$	$HCO_{3\,in}^-$ [cm^{-3}] $1.81 \cdot 10^{19}$	$HCO_{3\,out}^-$ [cm^{-3}] $1.20 \cdot 10^{19}$

Table 14. Data for the sodium-potassium pump in Section 7.

K_0^+ [cm^{-3}] $2.41 \cdot 10^{18}$	K_{in}^+ [cm^{-3}] $1.90 \cdot 10^{18}$	K_{out}^+ [cm^{-3}] $2.41 \cdot 10^{18}$
Na_0^+ [cm^{-3}] $8.19 \cdot 10^{19}$	Na_{in}^+ [cm^{-3}] $7.82 \cdot 10^{19}$	g_{Na^+} [cm^{-2}s^{-1}] $-6 \cdot 10^{19}$
Ca_0^{++} [cm^{-3}] $3.011 \cdot 10^{18}$	$g_{Ca^{++}}$ [cm^{-2}s^{-1}] $-2 \cdot 10^{19}$	Ca_{out}^{++} [cm^{-3}] $6.022 \cdot 10^{17}$
Cl_0^- [cm^{-3}] $7.17 \cdot 10^{19}$	Cl_{in}^- [cm^{-3}] $6.44 \cdot 10^{19}$	Cl_{out}^- [cm^{-3}] $7.89 \cdot 10^{19}$
$HCO_{3\,0}^-$ [cm^{-3}] $1.51 \cdot 10^{19}$	$HCO_{3\,in}^-$ [cm^{-3}] $1.81 \cdot 10^{19}$	$HCO_{3\,out}^-$ [cm^{-3}] $1.2 \cdot 10^{19}$

Table 15. Data for the calcium-sodium exchanger in Section 7.

K_0^+ [cm^{-3}] $2.41 \cdot 10^{18}$	$K^+{}_{in}$ [cm^{-3}] $1.90 \cdot 10^{18}$	$K^+{}_{out}$ [cm^{-3}] $2.41 \cdot 10^{18}$
Na_0^+ [cm^{-3}] $8.19 \cdot 10^{19}$	Na_{in}^+ [cm^{-3}] $7.82 \cdot 10^{19}$	$Na^+{}_{out}$ [cm^{-3}] $8.55 \cdot 10^{19}$
$Cl^-{}_0$ [cm^{-3}] $7.17 \cdot 10^{19}$	g_{Cl^-} [cm^{-2}s^{-1}] $+8 \cdot 10^{19}$	$Cl^-{}_{out}$ [cm^{-3}] $7.89 \cdot 10^{19}$
$HCO_{3\,0}^-$ [cm^{-3}] $1.81 \cdot 10^{19}$	$g_{HCO_3^-}$ [cm^{-2}s^{-1}] $-8 \cdot 10^{19}$	$HCO_{3\,out}^-$ [cm^{-3}] $1.20 \cdot 10^{19}$

Table 16. Data for the chloride-bicarbonate exchanger in Section 7.

K_0^+ [cm^{-3}] $2.41 \cdot 10^{18}$	K_{in}^+ [cm^{-3}] $1.90 \cdot 10^{18}$	K_{out}^+ [cm^{-3}] $2.41 \cdot 10^{18}$
Na_0^+ [cm^{-3}] $8.19 \cdot 10^{19}$	Na_{in}^+ [cm^{-3}] $7.82 \cdot 10^{19}$	g_{Na^+} [cm^{-2}s^{-1}] $-1.0 \cdot 10^{20}$
H_0^+ [cm^{-3}] $1.81 \cdot 10^{19}$	g_{H^+} [cm^{-2}s^{-1}] $-1.0 \cdot 10^{20}$	H_{out}^+ [cm^{-3}] $1.20 \cdot 10^{19}$
Cl_0^- [cm^{-3}] $7.17 \cdot 10^{19}$	Cl_{in}^- [cm^{-3}] $6.44 \cdot 10^{19}$	Cl_{out}^- [cm^{-3}] $7.89 \cdot 10^{19}$
$HCO_{3\,0}^-$ [cm^{-3}] $1.81 \cdot 10^{19}$	$HCO_{3\,in}^-$ [cm^{-3}] $1.81 \cdot 10^{19}$	$HCO_{3\,out}^-$ [cm^{-3}] $1.20 \cdot 10^{19}$

Table 17. Data for the sodium-proton exchanger in Section 7.

References

[1] P. Airoldi, A. G. Mauri, R. Sacco, and J. W. Jerome, *Three-dimensional numerical simulation of ion nanochannels*, J. Coupl. Sys. Multiscale Dyn. **3** (2015), no. 1, 57–65.

[2] B. Alberts, A. Johnson, J. Lewis, M. Raff, K. Roberts, and P. Walter, *Molecular biology of the cell*, 5th ed., Garland Science, New York, 2007.

[3] M. Z. Bazant, *Nonlinear electrokinetic phenomena*, Encyclopedia of microfluidics and nanofluidics (D. Li, ed.), Springer, 2008, pp. 1461–1470.

[4] _____, *Electrokinetics meets electrohydrodynamics*, J. Fluid Mech. **782** (2015), 1–4. MR Zbl

[5] Blausen Medical, *Medical gallery of Blausen Medical 2014*, WikiJ. Medicine **1** (2014), no. 2, art. id. 10.

[6] C. Breitkopf and K. Swider-Lyons (eds.), *Springer Handbook of electrochemical energy*, Springer, 2017.

[7] R. F. Brubaker, *Measurement of aqueous flow by fluorophotometry*, The glaucomas (R. Ritch, M. B. Shields, and T. Krupin, eds.), Mosby, St. Louis, 1989, pp. 337–344.

[8] D. Chen and R. Eisenberg, *Charges, currents, and potentials in ionic channels of one conformation*, Biophys. J. **64** (1993), no. 5, 1405–1421.

[9] _____, *Flux, coupling, and selectivity in ionic channels of one conformation*, Biophys. J. **65** (1993), no. 2, 727–746.

[10] T. C. Chu, O. A. Candia, and S. M. Podos, *Electrical parameters of the isolated monkey ciliary epithelium and effects of pharmacological agents*, Invest. Ophth. Vis. Sci. **28** (1987), no. 10, 1644–1648.

[11] D. F. Cole, *Electrical potential across the isolated ciliary body observed in vitro*, Brit. J. Ophthalmol. **45** (1961), 641–653.

[12] _____, *Transport across the isolated ciliary body of ox and rabbit*, Brit. J. Ophthalmol. **46** (1962), 577–591.

[13] B. Eisenberg, Y. Hyon, and C. Liu, *Energy variational analysis of ions in water and channels: field theory for primitive models of complex ionic fluids*, J. Chem. Phys. **133** (2010), no. 10, art. id. 104104.

[14] G. B. Ermentrout and D. H. Terman, *Mathematical foundations of neuroscience*, Interdisciplinary Applied Mathematics, no. 35, Springer, 2010. MR Zbl

[15] B. T. Gabelt and P. L. Kaufman, *Aqueous humor hydrodynamics*, Adler's physiology of the eye (P. L. Kaufman and A. Alm, eds.), vol. 8, Mosby, St. Louis, 1995, pp. 237–289.

[16] M. Goel, R. G. Picciani, R. K. Lee, and S. K. Bhattacharya, *Aqueous humor dynamics: a review*, Open Ophthalmol. J. **4** (2010), 52–59.

[17] B. Goldhagen, A. D. Proia, D. L. Epstein, and P. V. Rao, *Elevated levels of RhoA in the optic nerve head of human eyes with glaucoma*, J. Glaucoma **21** (2012), no. 8, 530–538.

[18] G. Guidoboni, A. Harris, J. C. Arciero, B. A. Siesky, A. Amireskandari, A. L. Gerber, A. H. Huck, N. J. Kim, S. Cassani, and L. Carichino, *Mathematical modeling approaches in the study of glaucoma disparities among people of African and European descents*, J. Coupl. Sys. Multiscale Dyn. **1** (2013), no. 1, 1–21.

[19] A. Heijl, M. C. Leske, B. Bengtsson, L. Hyman, B. Bengtsson, M. Hussein, and Early Manifest Glaucoma Trial Group, *Reduction of intraocular pressure and glaucoma progression: results from the Early Manifest Glaucoma Trial*, Arch. Opthalmol. **120** (2002), no. 10, 1268–1279.

[20] B. Hille, *Ion channels of excitable membranes*, 3rd ed., Sinauer, Sunderland, MA, 2001.

[21] M. Honjo, H. Tanihara, M. Inatani, N. Kido, T. Sawamura, B. Y. J. T. Yue, S. Narumiya, and Y. Honda, *Effects of rho-associated protein kinase inhibitor Y-27632 on intraocular pressure and outflow facility*, Invest. Ophth. Vis. Sci. **42** (2001), no. 1, 137–144.

[22] S. Iizuka, K. Kishida, S. Tsuboi, K. Emi, and R. Manabe, *Electrical characteristics of the isolated dog ciliary body*, Curr. Eye. Res. **3** (1984), no. 3, 417–421.

[23] M. Jaeger, M. Carin, M. Medale, and G. Tryggvason, *The osmotic migration of cells in a solute gradient*, Biophys. J. **77** (1999), no. 3, 1257–1267.

[24] J. W. Jerome, *Analytical approaches to charge transport in a moving medium*, Transport Theory Statist. Phys. **31** (2002), no. 4-6, 333–366. MR Zbl

[25] J. W. Jerome and R. Sacco, *Global weak solutions for an incompressible charged fluid with multi-scale couplings: initial-boundary-value problem*, Nonlinear Anal. **71** (2009), no. 12, e2487–e2497. MR Zbl

[26] G. Karniadakis, A. Beskok, and N. Aluru, *Microflows and nanoflows: fundamentals and simulation*, Interdisciplinary Applied Mathematics, no. 29, Springer, 2005. MR Zbl

[27] J. Keener and J. Sneyd, *Mathematical physiology*, Interdisciplinary Applied Mathematics, no. 8, Springer, 1998. MR Zbl

[28] J. W. Kiel, *Physiology of the intraocular pressure*, Pathophysiology of the eye: Glaucoma (J. Feher, ed.), Akademiai Kiadò, Budapest, 1998, pp. 109–144.

[29] J. W. Kiel, M. Hollingsworth, R. Rao, M. Chen, and H. A. Reitsamer, *Ciliary blood flow and aqueous humor production*, Prog. Retin. Eye Res. **30** (2011), no. 1, 1–17.

[30] J. W. Kiel, H. A. Reitsamer, J. S. Walker, and F. W. Kiel, *Effects of nitric oxide synthase inhibition on ciliary blood flow, aqueous production and intraocular pressure*, Exp. Eye Res. **73** (2001), no. 3, 355–364.

[31] T. Krupin, P. S. Reinach, O. A. Candia, and S. M. Podos, *Transepithelial electrical measurements on the isolated rabbit iris-ciliary body*, Exp. Eye Res. **38** (1984), no. 2, 115–123.

[32] H. H. Mark, *Aqueous humor dynamics in historical perspective*, Surv. Ophthalmol. **55** (2010), no. 1, 89–100.

[33] A. Mauri, A. Bortolossi, G. Novielli, and R. Sacco, *3D finite element modeling and simulation of industrial semiconductor devices including impact ionization*, J. Math. Ind. **5** (2015), art. id. 1. MR

[34] A. Mauri, R. Sacco, and M. Verri, *Electro-thermo-chemical computational models for 3D heterogeneous semiconductor device simulation*, Appl. Math. Model. **39** (2015), no. 14, 4057–4074. MR

[35] A. G. Mauri, L. Sala, P. Airoldi, G. Novielli, R. Sacco, S. Cassani, G. Guidoboni, B. Siesky, and A. Harris, *Electro-fluid dynamics of aqueous humor production: simulations and new directions*, J. Model. Ophthalmol. **1** (2016), no. 2, 48–58.

[36] R. A. Moses, *Intraocular pressure*, Adler's physiology of the eye: clinical application (R. A. Moses and W. M. Hart, eds.), Mosby, St. Louis, 1987, pp. 223–245.

[37] D. A. Neamen, *Semiconductor physics and devices*, McGraw-Hill, New York, 1997.

[38] H. A. Quigley and A. T. Broman, *The number of people with glaucoma worldwide in 2010 and 2020*, Brit. J. Ophthalmol. **90** (2006), 262–267.

[39] V. P. Rao and D. L. Epstein, *Rho GTPase/Rho kinase inhibition as a novel target for the treatment of glaucoma*, BioDrugs **21** (2007), no. 3, 167–177.

[40] Y. Rosenfeld, *Free-energy model for the inhomogeneous hard-sphere fluid mixture and density-functional theory of freezing*, Phys. Rev. Lett. **63** (1989), no. 9, 980–983.

[41] Y. Rosenfeld, M. Schmidt, H. Löwen, and P. Tarazona, *Fundamental-measure free-energy density functional for hard spheres: dimensional crossover and freezing*, Phys. Rev. E **55** (1997), no. 4, 4245–4263.

[42] R. Roth, *Introduction to density functional theory of classical systems: theory and applications*, lecture notes, Universität Stuttgart, 2006.

[43] R. Roth, R. Evans, A. Lang, and G. Kahl, *Fundamental measure theory for hard-sphere mixtures revisited: the White Bear version*, J. Phys. Condens. Mat. **14** (2002), no. 46, art. id. 12063.

[44] I. Rubinstein, *Electro-diffusion of ions*, SIAM Studies in Applied Mathematics, no. 11, SIAM, Philadelphia, 1990. MR

[45] R. Sacco, P. Airoldi, A. G. Mauri, and J. W. Jerome, *Three-dimensional simulation of biological ion channels under mechanical, thermal and fluid forces*, Appl. Math. Model. **43** (2017), 221–251. MR

[46] K. L. Schey, Z. Wang, J. L. Wenke, and Y. Qi, *Aquaporins in the eye: expression, function, and roles in ocular disease*, Biochim. Biophys. Acta **1840** (2014), no. 5, 1513–1523.

[47] M. Schmuck, *Analysis of the Navier–Stokes–Nernst–Planck–Poisson system*, Math. Models Methods Appl. Sci. **19** (2009), no. 6, 993–1015. MR Zbl

[48] M. Shahidullah, W. H. Al-Malki, and N. A. Delamere, *Mechanism of aqueous humor secretion, its regulation and relevance to glaucoma*, Glaucoma: basic and clinical concepts (S. Rumelt, ed.), InTech, London, 2011, pp. 3–32.

[49] M. B. Shields, *Study guide for glaucoma*, Williams & Wilkins, Baltimore, 1982.

[50] A. J. Sit, C. B. Nau, J. W. McLaren, D. H. Johnson, and D. Hodge, *Circadian variation of aqueous dynamics in young healthy adults*, Invest. Ophth. Vis. Sci. **49** (2008), no. 4, 1473–1479.

[51] J. A. Stratton, *Electromagnetic theory*, IEEE, Piscataway, NJ, 2007. Zbl

[52] M. Szopos, S. Cassani, G. Guidoboni, C. Prud'homme, R. Sacco, B. Siesky, and A. Harris, *Mathematical modeling of aqueous humor flow and intraocular pressure under uncertainty: towards individualized glaucoma management*, J. Model. Ophthalmol. **1** (2016), no. 2, 29–39.

[53] C. H. To, C. W. Kong, C. Y. Chan, M. Shahidullah, and C. W. Do, *The mechanism of aqueous humour formation*, Clin. Exp. Optom. **85** (2002), no. 6, 335–349.

[54] C. B. Toris, *Pharmacology of aqueous humor formation*, Encyclopedia of the eye (D. A. Dartt, ed.), Academic, Cambridge, MA, 2010, pp. 312–315.

[55] H. Tsukaguchi, T. Tokui, B. Mackenzie, U. V. Berger, X. Z. Chen, Y. Wang, R. F. Brubaker, and M. A. Hediger, *A family of mammalian Na+-dependent L-ascorbic acid transporters*, Nature **399** (1999), no. 6731, 70–75.

[56] A. Viswanathan, *Ocular biochemistry: tears, cornea, lens, aqueous, vitreous, retina and rhodopsin*, presentation, 2017.

[57] T. Watanabe and Y. Saito, *Characteristics of ion transport across the isolated ciliary epithelium of the toad as studied by electrical measurements*, Exp. Eye Res. **27** (1978), no. 2, 215–226.

[58] P. J. Wistrand, *Carbonic anhydrase in the anterior uvea of the rabbit*, Acta Physiol. Scand. **24** (1951), no. 2–3, 145–148.

[59] A. Wójcik-Gryciuk, M. Skup, and W. J. Waleszczyk, *Glaucoma: state of the art and perspectives on treatment*, Restor. Neurol. Neuros. **34** (2016), no. 1, 107–123.

[60] S. Yao, D. E. Hertzog, S. Zeng, J. C. Mikkelsen, Jr., and J. G. Santiago, *Porous glass electroosmotic pumps: design and experiments*, J. Colloid Interf. Sci. **268** (2003), no. 1, 143–153.

Received December 20, 2017. Revised December 6, 2018.

LORENZO SALA: sala@unistra.fr
Institut de Recherche Mathématique Avancée, Université de Strasbourg, CNRS, Strasbourg, France

AURELIO GIANCARLO MAURI: aureliogiancarlo.mauri@polimi.it
Dipartimento di Matematica, Politecnico di Milano, Milano, Italy

RICCARDO SACCO: riccardo.sacco@polimi.it
Dipartimento di Matematica, Politecnico di Milano, Milano, Italy

DARIO MESSENIO: dmessenio@virgilio.it
Eye Clinic, Department of Clinical Science, ASST Fatebenefratelli Sacco, University of Milan, Milan, Italy

GIOVANNA GUIDOBONI: guidobonig@missouri.edu
Department of Electrical Engineering and Computer Science, University of Missouri, Columbia, MO, United States

ALON HARRIS: alharris@indiana.edu
Eugene and Marilyn Glick Eye Institute, Indiana University School of Medicine, Indianapolis, IN, United States